Potential role of volcanic glass-smectite mixtures in slow earthquakes in shallow subduction zones: Insights from low- to high-velocity friction experiments

Hanaya Okuda[1,2,*], Takehiro Hirose[3], Asuka Yamaguchi[1,2]

[1] Department of Ocean Floor Geoscience, Atmosphere and Ocean Research Institute, University of Tokyo, Japan

[2] Department of Earth and Planetary Science, University of Tokyo, Japan

[3] Kochi Institute for Core Sample Research (X-star), Japan Agency for Marine-Earth Science and Technology (JAMSTEC), Japan

* Corresponding author: Hanaya Okuda (okuda@aori.u-tokyo.ac.jp)

Abstract

Volcanic glass and its mixture with smectite are commonly observed in shallow parts of subduction zones. As volcanic glass layers often act as a glide plane to induce mass transportation such as submarine landslides, and because its alteration product, smectite, is one of the frictionally weakest geological materials, the frictional characteristics of volcanic glass-smectite mixtures are important for fault slip behavior in shallow parts of subduction zones. We performed a series of friction experiments on volcanic glass-smectite mixtures with different smectite contents at various velocity conditions from 10 μm/s to 1 m/s under an effective normal stress of 5 MPa and pore pressure of 10 MPa. In general, friction coefficients negatively depend on the smectite content at any velocity tested. We found that samples with smectite contents of 15-30 % showed a drastic slip-weakening behavior at intermediate velocities of 1-3 mm/s with a characteristic slip displacement of ~0.1 m. Finite element method modeling shows that thermal pressurization does not contribute to the observed weakening behavior. We propose that gouge fluidization or compaction-induced pore pressure increase may be the cause of the weakening. The slip-weakening behavior at intermediate velocities enlarges a critical nucleation length for frictional instability to 1-30 km, or prevent acceleration to seismic slip velocities. Therefore, gouges with minor amount of clay, such as subducting volcanic ash layers, may contribute to the occurrence of the slow earthquakes at shallow depths in subduction zones.

Plain language summary

Materials erupted from volcanoes deposit on the seafloor and subduct at the trench. One such material, volcanic glass, easily turns into mechanically weak clay minerals such as smectite that can cause an enormous slip during an earthquake in subduction zones. In this study, we experimentally examined the frictional properties of mixtures of volcanic glass and smectite to elucidate fault slip behavior in shallow depths of subduction zones. Experiments with varying smectite content showed that a drastic reduction in fault frictional strength was induced when a small amount of smectite was present at moderately high velocity conditions. This behavior may induce slow earthquakes that could be related to huge earthquakes in subduction zones.

Key points

- Small amount of clay mineral induces a drastic slip-weakening at ~1 mm/s.
- Thermal processes do not contribute to the weakening behavior.
- Slip-weakening enlarges critical nucleation length leading to slow earthquakes.

1. Introduction

In subduction zones, the downgoing slab provides fluids to the upper plate leading to melt production and the formation of arc volcanoes. Erupted materials from these arc volcanoes, which mainly consist of volcanic glass, deposit on the incoming plate and subduct at the trench as ash layers or dispersed ash in the incoming sediment (Screaton et al., 2009). At the Nankai Trough, for example, approximately 35% of the incoming sediment is of volcanic origin (Scudder et al., 2018). As volcanic glass reacts

progressively with water to form smectite through diagenetic and weathering processes (Compton, 1991), and because smectite is frictionally weak (Morrow et al., 2017), the frictional properties of volcanic glass-smectite mixtures are important for understanding natural hazards associated with subduction zones and volcanic regions, such as earthquakes and landslides. For example, hemipelagic smectite may have been responsible for the large fault slip that occurred near the trench during the 2011 Tohoku-Oki earthquake at the Japan Trench (Chester et al., 2013; Ujiie et al., 2013), with the smectite originating from altered volcanic glass that was deposited on the northwestern part of the Pacific Plate (Kameda et al., 2015). Seismic fault behavior can also occur in these volcanic materials during caldera collapse or magma ascent (Han et al., 2019; Lavallée et al., 2014), and volcanic ash layers may also act as glide planes for subaqueous and terrestrial landslides (Wiemer & Kopf, 2017). Such examples of ash layers at the base of the mass-transport deposits have been reported at the Nankai Trough (Laberg et al., 2017; Strasser et al., 2012), the Middle America Trench (Harders et al., 2010) and Lake Villarrica in Chile (Wiemer et al., 2015), as well as for terrestrial landslides in New Zealand and Japan (Kluger et al., 2020; Moon, 2016; S. Nakamura et al., 2014; Shimizu & Ono, 2016).

Despite its potentially important role in natural hazards, our understanding of the frictional behavior of volcanic glass-smectite mixtures is limited. Previous experimental studies have shown that volcanic glass has friction coefficients of 0.6-0.8 at low velocity conditions less than 1 mm/s (Lavallée et al., 2014; Wiemer & Kopf, 2015), consistent with “Byerlee's rule” for rock friction (Byerlee, 1978). When it is mixed with smectite, the frictional strength of the glass-smectite mixture shows an

inverse relationship with smectite content (Wiemer & Kopf, 2015), similar to other previous results where weak clay minerals have been mixed with non-clay minerals (Bedford et al., 2022; Ikari et al., 2018; Logan & Rauenzahn, 1987; Okuda et al., 2021; Takahashi et al., 2007; Tembe et al., 2010). At a high slip-velocity up to 1.3 m/s, the frictional strength of volcanic glass is dynamically weakened (Lavallée et al., 2014). As for smectite, a low friction coefficient of 0.1-0.2 under wet conditions has been reported at low sliding velocities (Morrow et al., 2017). Friction is also low at high sliding velocities, but thermal pressurization additionally plays a significant role in the weakness of wet smectite during high velocity slip (Faulkner et al., 2011; Ujiie & Tsutsumi, 2010). Although we have some constraints on the individual frictional behaviors of smectite and volcanic glass from the previous studies mentioned above, there is a lack of data on their frictional behavior when they are mixed together and sheared over a range of velocity conditions, particularly intermediate velocities of an order of 1 mm/s.

To understand better the frictional behavior of volcanic glass-smectite mixtures, we performed a series of friction experiments from low to high velocity under controlled pore pressure conditions. Based on the obtained frictional properties of glass-smectite mixtures, we discuss the implications for fault slip behavior at shallow subduction zones where volcanic glass is abundant (e.g., the Nankai Trough, SW Japan).

2. Method

2.1. Materials

Volcanic glass samples erupted from the Baekdusan volcano in the North Korea,

collected at the southern part of Hokkaido, Japan (Y. Nakamura, 2016; Nakanishi et al., 2020), were used for experiments. This volcanic glass has been used as a chronological marker of the eruption at Baekdusan volcano in 10^{th} century, and few minerals other than glass are present after being transported over 1000 km (Y. Nakamura, 2016). Samples were sieved to obtain particle sizes between 63-250 μm. The broad halo without significant peaks in the XRD profile indicates the sample has little impurity and is predominantly comprised of amorphous glass (Figure 1a). Scanning electron microscope (SEM) images shows that the glass consists of angular shards (Figure 1a). For the smectite sample, we used commercially available purified smectite ("Kunipia-F" provided by Kunimine Industries Co. Ltd., Japan), comprised of montmorillonite with less than 2% quartz as an impurity. Mean grain size is reported to be 2.5 μm, but particle aggregates can be several hundred micrometers in diameter (Figure 1b). No disaggregation procedure was employed. We prepared 10 g testing samples for each experiment by mixing volcanic glass and smectite with different gravimetric smectite content under room dry condition (Table 1).

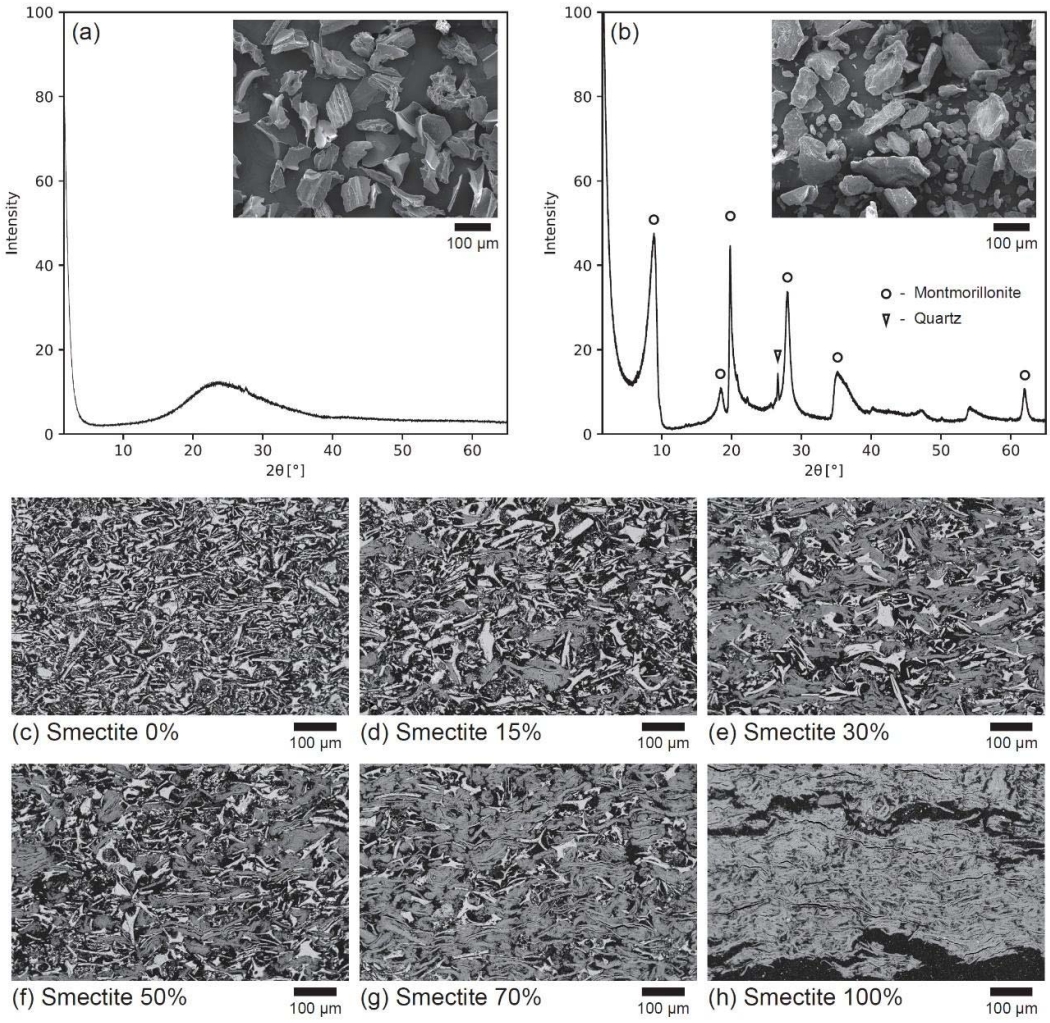

Figure 1.

XRD profiles and SEM micrographs for (a) volcanic glass and (b) smectite. (c-h) Unsheared microstructures (SEM backscattered electron images) for each tested clay mineral content after applying the effective normal stress of 5 MPa. Bright, angular grains are volcanic glass particles, dark areas are smectite particles, and black areas are epoxy resin.

2.2. Experimental procedure

Friction experiments were conducted using the pressurized high-velocity (PHV) rotary shear apparatus located in Kochi Institute for Core Sample Research, JAMSTEC, Japan (Figure 2a, Tanikawa et al., 2012, 2015). Experimental samples were inserted into the hollow cylindrical sample chamber (outer and inner diameters of 60 and 30 mm, respectively) and sandwiched between metal porous spacers. The samples are confined by Teflon liners and O-rings. The initial thickness of the gouge layer was about 4.5 mm for the 100% glass sample and 2 mm for the 100% smectite sample. Pore water was introduced to the gouge through both the upper and lower porous spacers (Rempe et al., 2017). Pore fluid pressure (P_f) was kept constant at a value of 10 MPa during the experiments and changes in the pore water volume (e.g., due to compaction/dilation) were monitored by the pore pressure generator. Temperature (T) was measured just above the gouge layer by a metal-sheathed thermocouple. Normal stress (σ_n) was applied from the upper loading side to keep an effective normal stress (σ_{eff}) of 5 MPa to simulate the pressure conditions experienced in the shallow regions of subduction zones. The shear stress (τ) was applied by the lower rotational side. As the slip velocity (V) varies depending on the distance from the rotation axis, we use the "equivalent" velocity (V_{eq}) for the representative V (Shimamoto & Tsutsumi, 1994) defined as follows:

$$V_{eq} = \frac{4\pi R(r_o^2 + r_o r_i + r_i^2)}{3(r_o + r_i)}, \#(1)$$

where R is the revolutions rate, r_o and r_i are the inner and outer radii of the hollow cylindrical specimen, which are 15 and 30 mm, respectively. In most tests, V_{eq} was initially set to be 100 μm/s for the first 300 mm of shear displacement (nominally "pre-

150 slip"), and then reduced to 10 μm/s followed by stepwise increases by a factor of 3 up to
151 300 mm/s ("multi-V test"). Acceleration and deceleration rates were set to be 0.5 m/s^2.
152 Before stepping from 3 mm/s to 10 mm/s, rotation was stopped for a short time to shift
153 from the slow gear to the fast gear. During rotation with the slow gear, the acceleration
154 rate during the velocity steps is quick enough to be regarded as an abrupt change in $V_{eq,}$
155 up to the step from 1 mm/s to 3 mm/s where the acceleration phase finished in less than
156 0.004 s. Shear displacements were set to be 15 mm for V_{eq} = 10-300 μm/s, 150 mm for
157 V_{eq} = 1 and 3 mm/s, 1.5 m for V_{eq} = 10 and 30 mm/s, and 4.5 m for V_{eq} = 100 and 300
158 mm/s (Figure 2b). For samples with smectite contents of 0, 15, and 70%, experiments
159 with low V_{eq} from 10 μm/s to 3 mm/s were also conducted (PHV596, 592, and 595;
160 "low-V test"). For the 15%-smectite sample, V_{eq} was reduced to 10 μm/s after it reached
161 to 3 mm/s, and then increased again to 3 mm/s (PHV592). Additional tests for 100%-
162 smectite and 100%-glass samples were conducted with V_{eq} of 1 m/s for 12.5 m after the
163 pre-slip of 300 mm with V_{eq} = 1 mm/s (PHV593 and 594; "single-velocity test"). Test
164 conditions are summarized in Table 1. Friction coefficient μ is calculated by dividing τ
165 with σ_{eff}. The τ value between Teflon liner and O-ring was less than 0.15 MPa under P_f
166 = 10 MPa conditions at V_{eq} < 3 mm/s; no correction for the seal friction was applied.
167 Axial displacement, volume of pore water expelled from the gouge, and T in the vicinity
168 of the gouge were measured during experiments to evaluate the gouge thickness and
169 fluid expulsion. All experimental data were collected at a sampling rate of 100 Hz.
170

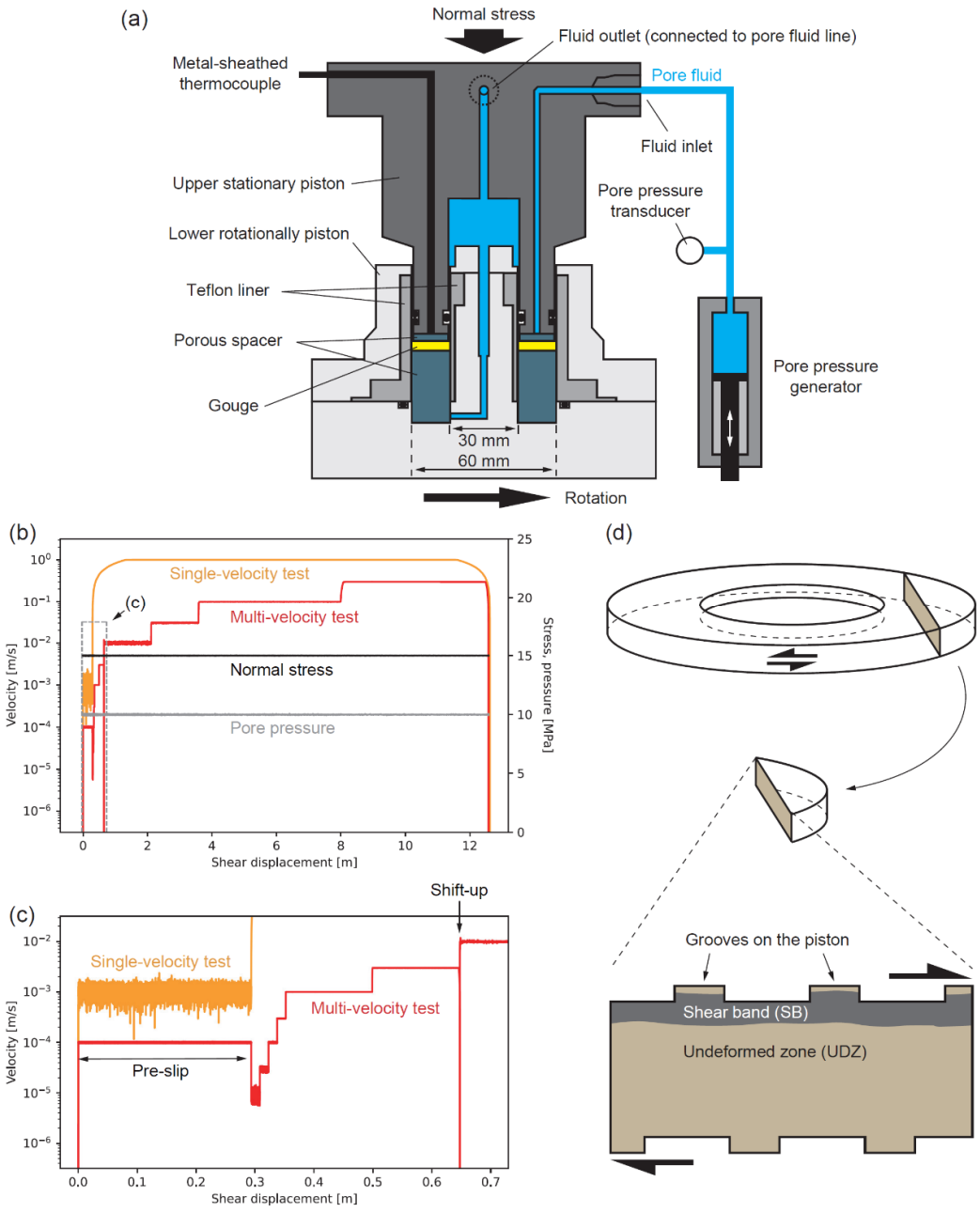

171

172 **Figure 2.**

173 (a) Schematic view of the experimental configuration. (b and c) Velocity sequences

174 employed in this study. (d) Location for the microstructural observation and the

175 schematic deformation texture.

176

177 **Table 1.**

178 List of experiments in this study.

Run	Glass / smectite [%]	V_{eq} [m/s]	Displacement [m]	Comment
PHV591	100 / 0	10^{-5} – $10^{-0.5}$	13	Multi-*V* test
PHV586	85 / 15	10^{-5} – $10^{-0.5}$	13	Multi-*V* test
PHV587	70 / 30	10^{-5} – $10^{-0.5}$	13	Multi-*V* test
PHV588	50 / 50	10^{-5} – $10^{-0.5}$	13	Multi-*V* test
PHV589	30 / 70	10^{-5} – $10^{-0.5}$	13	Multi-*V* test
PHV590	0 / 100	10^{-5} – $10^{-0.5}$	13	Multi-*V* test
PHV593	100 / 0	10^{0}	13	Single-*V* test
PHV594	0 / 100	10^{0}	13	Single-*V* test
PHV592	85 / 15	10^{-5} – $10^{-2.5}$	1.2	Low-*V* test with additional *V* steps
PHV595	30 / 70	10^{-5} – $10^{-2.5}$	0.7	Low-*V* test
PHV596	100 / 0	10^{-5} – $10^{-2.5}$	0.7	Low-*V* test

179

180 **2.3. Microstructural observations**

181 After the experiments, gouge samples were retrieved from the apparatus and
182 impregnated with epoxy resin so they could be cut and polished to obtain cross-
183 sectional microstructural images normal to the gouge layer and subparallel to the shear

direction (Figure 2d). The microstructural images were acquired at the Atmosphere and Ocean Research Institute (University of Tokyo, Japan) using a JEOL JXA-8900 scanning electron microscope (SEM) with an accelerating voltage of 15 kV. As it was difficult to recover the entire sample due to the unconsolidated nature of the gouge, we focused our observations on the structures in the vicinity of the shear band that forms near the edge of the gouge layer (SB, Figure 2d), where the shear deformation is localized compared to surrounding undeformed zone (UDZ, Figure 2d).

2.4. Finite Element Method (FEM) modeling

To constrain the T and P_f conditions inside the gouge, we used COMSOL Multiphysics® software and modeled time-dependent heat transfer and fluid diffusion which follow the equations below (Rice, 2006):

$$\frac{\partial T}{\partial t} = \frac{1}{\rho_g C_p}\nabla(K\nabla T) + \frac{A(r)}{\rho_g C_p}, \#(2)$$

$$\frac{\partial P_f}{\partial t} = \frac{1}{\rho_f \phi(\beta_f + \beta_\phi)}\nabla\left(\frac{\rho_f k}{\eta_f}\nabla P_f\right) + \frac{(\gamma_f - \gamma_\phi)}{(\beta_f + \beta_\phi)}\frac{\partial T}{\partial t}, \#(3)$$

where t is time, ρ_f is water density, ρ_g is density of a material, C_p is heat capacity of a material, K is thermal conductivity of a material, γ_f is water thermal expansivity, γ_ϕ is pore space thermal expansivity, β_f is water compressibility, β_ϕ is pore space compressibility, ϕ is porosity, η is water viscosity, k is permeability (see Table 2 for details). We assume $k = 10^{-20}$ m^2 to simulate the low permeability nature of clay-mixed gouge (Oohashi et al., 2015; Takahashi et al., 2007). $A(r)$ is heat generation per unit volume at the distance from the rotation axis r calculated as follows:

$$A(r) = \frac{1}{w_{hs}} V(r)\tau = \frac{1}{w_{hs}} \left(\frac{3}{4}(2r) \frac{r_o + r_i}{r_o^2 + r_o r_i + r_i^2} V_{eq} \right) \tau, \#(4)$$

where w_{hs} is thickness of the heat source where shear localized within the gouge and $V(r)$ is velocity at r. We assumed that τ is independent of r within the limited velocity range from $V(r_i) = 0.64V_{eq}$ to $V(r_o) = 1.29V_{eq}$. Dilation/compaction of the gouge and thermoelastic response of the apparatus are not considered in the FEM modeling.

A schematic representation of FEM configuration is shown in Figure 3. The model was made using the axial symmetry, thus only one side of the gouge layer shown. Fluid diffusion (equation 3) is only considered inside the gouge zone with thickness of 2 mm. We set the initial P_f conditions throughout the entire gouge layer to be 10 MPa, and the P_f was fixed at this value at the top and bottom boundaries of the gouge layer (Dirichlet boundary condition). The inner and outer boundaries have no flow of fluid crossing the boundaries. Based on microstructural observations, the heat source inside the gouge was assumed to be concentrated in the shear localized zone (SB) with w_{hs} = 0.3 mm at 0.1 mm below the top of gouge. We extract T data at r = 22.5 mm at a distance of 1 mm above the gouge layer and compare it with the measured T during experiments. For simplicity, shear forces between O-rings and Teflon liners and the frictional heat generated from the outer and inner contacts are ignored in the FEM model. Based on the computed P_f inside the heat source where shear localized, we define P_{feq} which represents the "equivalent" influence of P_f on frictional behavior as follows (see Appendix A1 for details):

$$P_{feq} = \frac{3}{r_o^3 - r_i^3} \int_{r_i}^{r_o} \int_{z_{hs}^{bot}}^{z_{hs}^{top}} \frac{P_f(r,z) r^2}{w_{hs}} dz\, dr, \#(5)$$

where $P_f(r, z)$ is the calculated P_f at r and z (direction vertical to the gouge) inside the

shear localized zone, z_{hs}^{top} and z_{hs}^{bot} are z for top and bottom ends of the shear localized zone, respectively, thus $w_{hs} = z_{hs}^{top} - z_{hs}^{bot}$. Equation 5 leads to:

$$\mu_{obs}(\sigma_n - P_{fo}) = \mu_{cor}(\sigma_n - P_{feq}), \#(6)$$

where μ_{cor} is the corrected μ value without the influence of pore pressure variation due to frictional heat, and P_{fo} is the imposed P_f (= 10 MPa in this study).

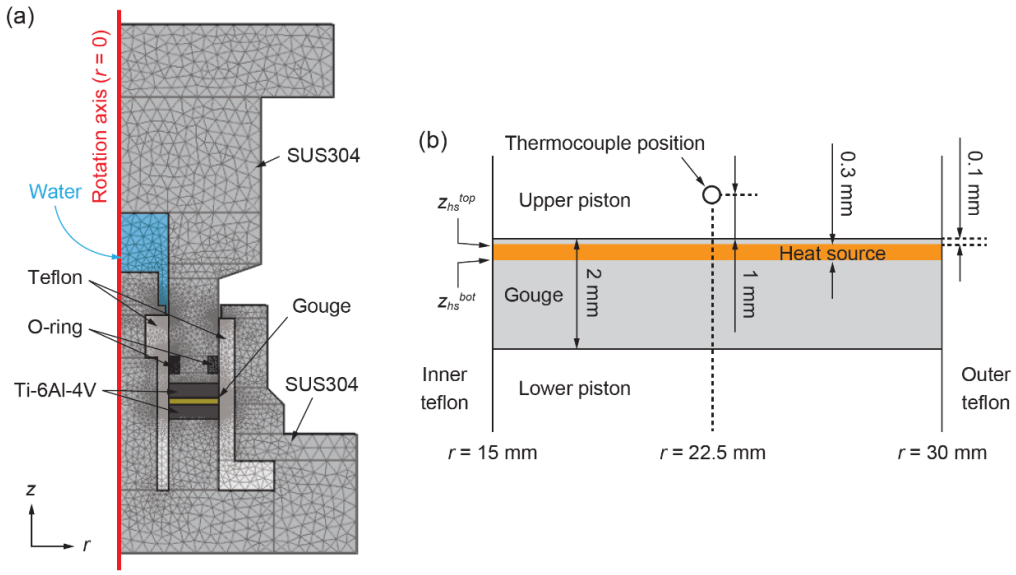

Figure 3.

(a) Geometry and mesh structure for the FEM modeling. (b) Close up view of the gouge with locations of heat source and the thermocouple.

Table 2.

Mechanical properties of components in the FEM model at around room temperature. Dependence on temperature was employed for the parameter with an asterisk.

	Gouge	Pore space	SUS304	Ti-6Al-4V	Teflon	O-ring	Water

ρ [kg/m^3]	2400		*7900	*4420	2200	1800	*1004
C_p [J/kg/K]	1000		*462	*546	1050	1500	*4216
K [W/m/K]	1.5		*14.6	*7	0.25	0.3	*0.56
γ [1/K]		2.4×10^{-5}					5.7×10^{-4}
β [1/Pa]		2.49×10^{-9}					0.49×10^{-9}
ϕ	0.25						
η [Pa.s]							*1.8×10^{-3}
k [m^2]	10^{-20}						

3. Results

3.1. Steady state friction coefficient

Results on frictional strength at all V_{eq} conditions are summarized in Figures 4 and S1. Friction coefficients (μ) of 100%-glass sample ranged from 0.6 to 0.7 with a V-strengthening behavior from V_{eq} = 10 μm/s to 30 mm/s. At V_{eq} = 100 mm/s, μ dynamically weakened from a peak value of 0.8 to a steady state value of 0.2. Such a low μ is also observed at a V_{eq} of 300 mm/s in the multi-V test (Figure 4a) and 1 m/s in the single-V test (Figure 4b).

As smectite content was increased, frictional strength decreased at every V condition. For samples with 15 and 30% smectite, at $V_{eq} \leq$ 300 μm/s, steady state μ values were about 0.5 and 0.3, respectively, with V-neutral or slightly V-weakening trends. At V_{eq} = 1-3 mm/s (intermediate V range), μ decreased to 0.1-0.2 with a

249 characteristic weakening time or distance (see section 3.2) and remained low at higher
250 V_{eq} conditions (Figures 4a and 4c). For samples with more than 50% smectite, μ was as
251 low as 0.1 at every V_{eq} condition, with nearly V-neutral trends.
252 According to the FEM modeling (section 3.4), at high-V and low-μ conditions (V
253 $> 10^{-2}$ m/s and $\mu < 0.3$), the measured μ may be significantly overestimated by friction
254 between O-ring and Teflon liners. However, it is difficult to estimate exact effect of the
255 seal friction because the amount of gouge materials that extrude from the layer and fill
256 the space between upper and lower pistons and inner and outer Teflon liners may vary
257 with experimental conditions, such as velocity, displacement, and mineral compositions.

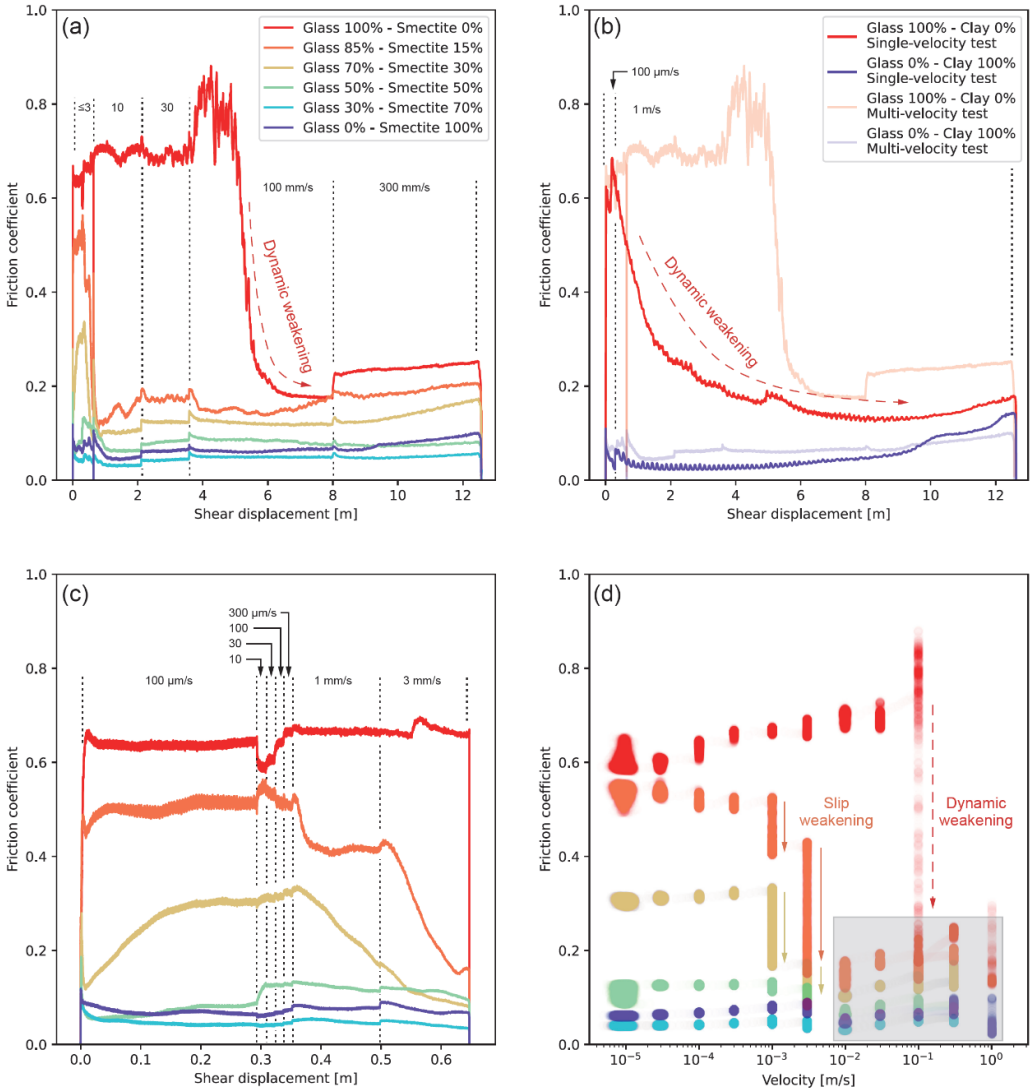

Figure 4.

(a) Mechanical behavior of multi-V tests (V_{eq} = 10 μm/s to 300 mm/s) with different smectite contents. (b) Results of single-V tests (V_{eq} = 1 m/s) for 100%-glass and 100%-smectite cases. Light colors represent the results of multi-V tests and dark colors represent those of single-V tests. (c) Close view of the low-V (V_{eq} < 3 mm/s) part of multi-V tests shown in (a). (d) Relation between μ and V_{eq} for multi-V and single-V tests (V_{eq} = 1 m/s) after the pre-slip stage. Single-V tests were only conducted for the smectite

266 contents of 0 and 100%. Gray area indicates a possible range where friction coefficients
267 are overestimated due to the seal friction.
268
269 **3.2. Frictional behavior for a sample with 15% smectite at low to intermediate**
270 **velocity range**
271 To see if the observed weakening behavior for 15%- and 30%-smectite samples
272 at the intermediate V range depend on V_{eq} or on shear strain, we performed an additional
273 experiment (PHV592, 15% smectite) that included both velocity upsteps and downsteps.
274 We found that μ recovered to 0.5 during the V downsteps which is consistent with μ in
275 the low V range before the V upsteps (Figure 5). μ decreased again in the subsequent V
276 upsteps, which implies that the steady-state μ in the intermediate V range is independent
277 of shear strain and only dependent on V.
278 Just after the V step, μ showed a positive spike followed by a gentle increase
279 and then a decrease to its steady state μ at each V condition (Figures 5b-e). The spikes
280 appear to be comprised of a direct effect and an evolutionary effect described by the
281 rate- and state-dependent friction (RSF) law (Figures 5f-i) (Dieterich, 1979; Ruina,
282 1983). The evolutionary effect has a characteristic slip distance of ~100 μm. The extent
283 of the increase in μ after the RSF-like behavior seems to be positively related to the
284 imposed V_{eq} conditions, except for the V step from V_{eq} = 1 mm/s to 3 mm/s, although
285 the V steps may be affected by the P_f condition at these slip rates (gray markers in
286 Figures 5b-e; see section 3.4). Little variation in gouge thickness during the V steps was
287 observed (Figures 5b-i). As the V step was imposed within less than 0.004 seconds, and
288 because the gentle increase and decrease in μ occurred after the direct and evolutionary

effects, the observed weakening behavior at the intermediate V range to μ = 0.1-0.2 is not a response to V step (like the RSF law) but a slip-weakening behavior toward the steady state μ value for a given V condition. During this behavior, gouge thickness did not vary, whereas the thermocouple captured gentle increases in T especially at V_{eq} = 1 and 3 mm/s (section 3.4).

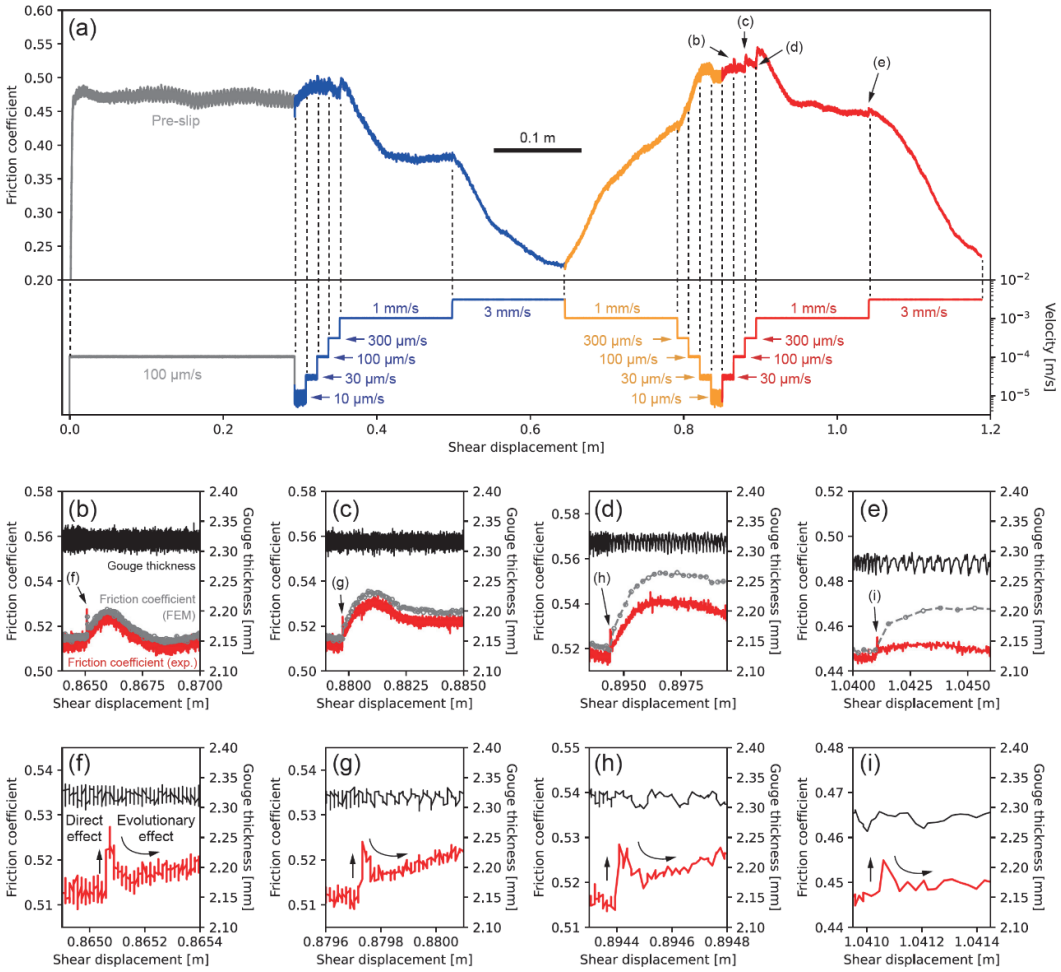

Figure 5.

(a) Experimental result of PHV592 (15% smectite, low-velocity test with additional

298 velocity steps). (b-i) Close-up views of variation in friction coefficient at the velocity
299 steps for PHV592. Red lines are experimental data and gray lines in (b-e) are modeled
300 friction coefficient by FEM after correcting pore pressure effect, and black lines are
301 gouge thickness.
302
303 **3.3. Microstructure**
304 Before imposing shear deformation, volcanic glass grains kept their original,
305 angular shapes regardless of the smectite content (Figure 1). As the smectite content
306 was increased, volcanic glass grains distributed in the smectite matrix and the numbers
307 of contacts between glass grains reduced. After the shear deformation, samples often
308 showed a localized shear band (SB) in the upper part of the gouge layer, characterized
309 by grain size reduction and an increase in the number of rounded grains compared to the
310 surrounding undeformed zone (UDZ).
311 The thickness of the SB for the 100%-glass sample sheared at low-V (PHV596,
312 Figures 6a-c) was about 300 μm, with the SB containing more rounded grains than the
313 UDZs. The mean grain size in the SB was less than ~50 μm, with the minimum grain
314 size being <1 μm (Figure 6c).
315 For the sample with V_{eq} up to 300 mm/s (PHV591, Figures 6d-f), the SB had a
316 similar thickness as the low-V sample (PHV596), however a localized shear band (LSB)
317 with a thickness of 10-20 μm had also formed in the middle of the main SB (Figure 6f).
318 The largest grain size in the LSB was <1 μm, which was significantly smaller than the
319 surrounding SB. The mean grain size in the main SB was several tens of microns, which
320 was a little smaller than that in the SB of the low-V sample (PHV596). In some portions

321 of the SB and UDZ, larger fragments (FR; Figures 6d and 6e) containing features that
322 look like LSBs were observed, possibly indicating reworking of localized bands that
323 formed during previous *V*-steps in the multi-*V* test.

324 For low-smectite samples (e.g., 15%-smectite, PHV592, low-*V* test), a SB was
325 also observed, however it was a little wider (~500 μm) than 100%-glass case (Figure
326 6g). The grain size of glass particles was reduced to less than 50 μm (Figure 6h). The
327 grain shape appeared to be a little more angular than 100%-glass case (Figure 6i), and
328 the crushed glass particles were dispersed and mixed with smectite (Figure 6i).

329 For high-smectite samples, no SB was observed (Figure 6j). No obvious
330 localized feature was observed for the 70%-smectite sample (PHV589) and one shear
331 plane parallel to the deformation was likely observed for 100%-smectite sample
332 (PHV590), although it is potentially an unloading feature. Glass grains in the 70%-
333 smectite sample were not in contact with each other and preserved their original angular
334 shapes and sizes (Figures 1, 6h, and j). As the size of smectite particles was less than 2
335 μm, we could not easily resolve the deformation within the smectite matrix, although
336 the deformation may be primarily accommodated by smectite matrix.
337

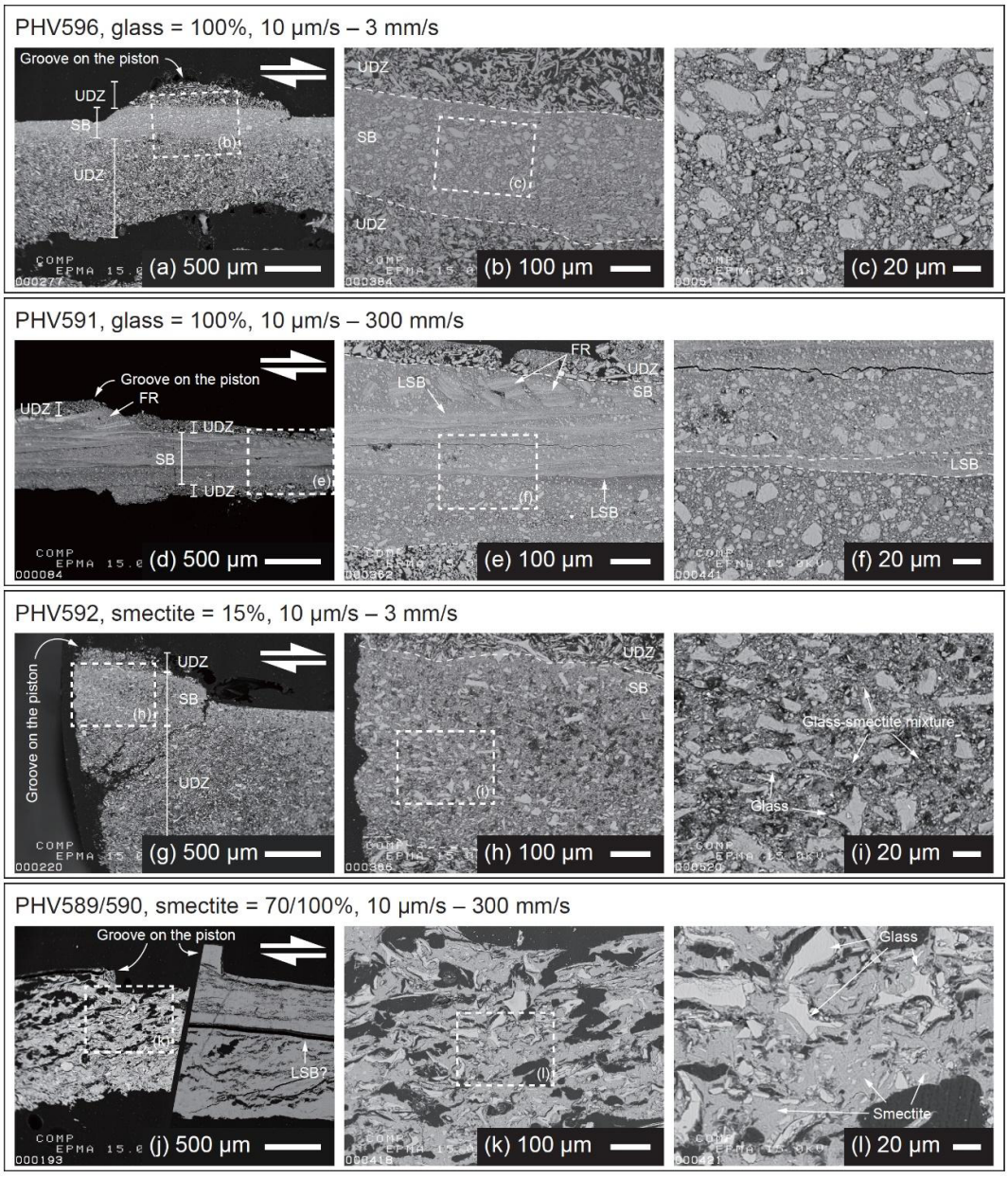

Figure 6.

Microstructures of deformed samples for (a-c) 100%-glass with low-*V* test of PHV596, (d-f) that with multi-*V* test of PHV591, (g-i) 15%-smectite with low-*V* test of PHV592, and (j-l) 70%- or 100%-smectite with multi-*V* tests of PHV589 or 590. The left side of (j) is the microstructure for PHV589 (70% smectite) and the right one is that for

PHV590 (100% smectite). Locations of figures in the center and right columns are shown in the left and center columns, respectively. SB: shear band; UDZ: undeformed zone; LSB: localized shear band; FR: fragment.

3.4. Temperature and pore pressure conditions inside the gouge

In the FEM modeling, we obtained fairly consistent result of T with the measured value for the low-V tests (Figure 7a). The modeled maximum T increase within the gouge is 12°C for 100%-glass, 6-7°C for 85%-glass, and less than 3°C for <70%-glass samples (Figure 7b). For the 100%-glass sample at high-V conditions, the modeled T at the thermocouple position showed consistent result with measured T, at least for shear displacements of <5 m, which is before the friction dynamically weakened (Figure 7c, see also Figure 4a). The maximum T inside the gouge reached about 340°C when the shear displacement was 5 m, which was the onset of dynamic weakening (Figure 7d). After the dynamic weakening behavior, the modeled T was significantly overestimated, which implies a significant shear resistance between the O-rings and Teflon liners at high-V conditions. Such a discrepancy between modeled and measured T conditions was also observed for high-V conditions with other samples. Hence, the μ of the gouge may be nearly zero at high-V conditions, but as we cannot know the true μ as a result of the contribution from O-ring and Teflon friction, we do not discuss the friction values in detail at the V conditions of the shaded region in Figure 4d.

The distribution of P_f within the gouge was simultaneously modeled in the FEM modeling. In the case of PHV592 (15% smectite), the maximum T increase was only 6-

7°C (Figure 7b) because of slow V and relatively low μ, meaning T within the gouge is far lower than the boiling T of water at P_f = 10 MPa (Figure 8c). However, the low permeability nature of the clay-mixed gouge ($k = 10^{-20}$ m^2) caused an increase in P_f inside the gouge of up to 0.3 MPa (Figure 8e), with P_{feq} being about 10.2 MPa just after the V-step from V_{eq} = 1 to 3 mm/s (Figure 8a). This P_f build-up caused a reduction in σ_{eff} (Figure 8a) and thus the measured μ was apparently lowered. We corrected the μ in PHV592 by using equations 5 and 6 and found that the measured μ value just after the V-steps from V_{eq} = 1 to 3 mm/s was underestimated by about 0.02 (Figure 5e), however this is insufficient to explain the slip-weakening behavior we observe (Figure 8b).

The P_f conditions inside the gouge are also influenced by gouge compaction and dilation, which are not implemented in the FEM modeling. As shear displacement increased during the test, gouge thickness reduced as measured by the shortening in the axial displacement data. The majority of axial shortening occurred during the pre-slip stage, but gouge thickness continuously decreased afterward (Figure 8c). However, the volume of expelled water was consistent with the amount of axial shortening (ideally, the volume of expelled water [cc] = 0.001 [cc/mm^3] × (30 [mm])^2 × π × axial shortening [mm]), suggesting that the P_f build up due to the gouge compaction would be minimal. Furthermore, gouge compaction occurred simultaneously with the slip-hardening in the V downsteps. Therefore, the influence of gouge compaction on P_f is likely to be insignificant and not a dominant cause of the observed slip-weakening behavior and low steady state μ values at V_{eq} = 1 and 3 mm/s.

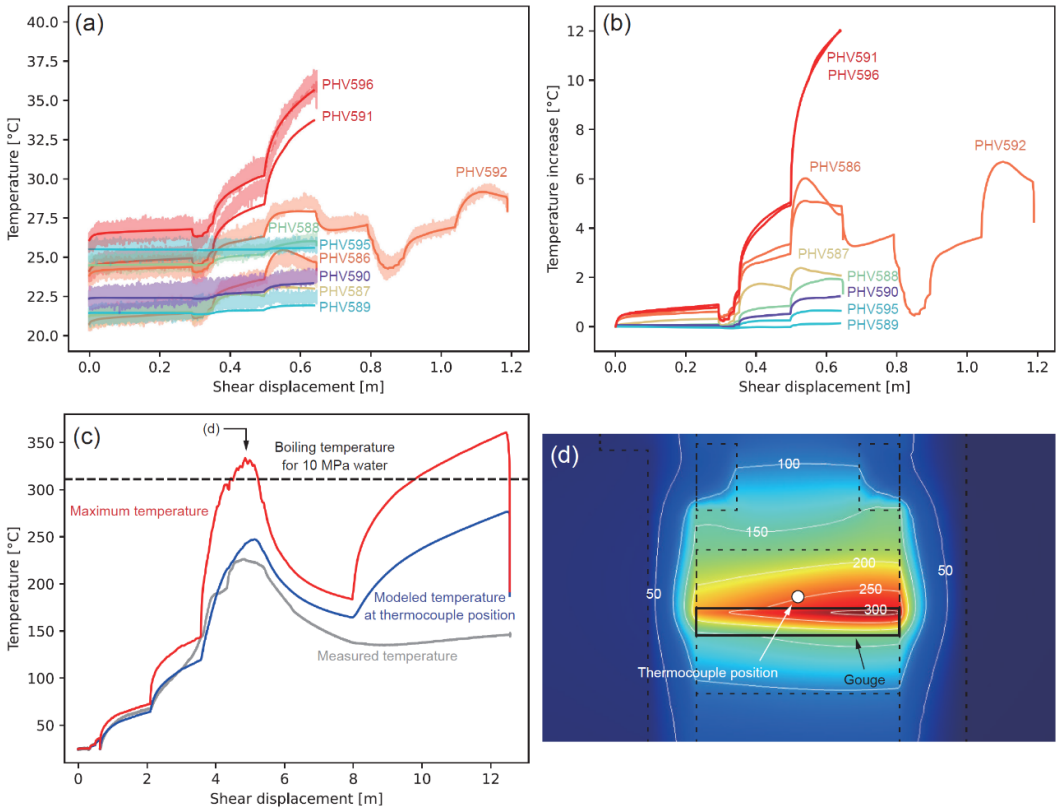

Figure 7.

(a) Measured *T* (light color) and modeled *T* (solid line) at the thermocouple position for low-*V* conditions. (b) Modeled maximum *T* increase within the gouge for low-*V* conditions. (c) Measured *T* (gray), modeled *T* at the thermocouple position (blue) and the maximum *T* inside the gouge (red) for high-*V* conditions of PHV591 (glass 100%). (d) Distribution of *T* around the gouge at the shear displacement of ~5 m indicated in (c).

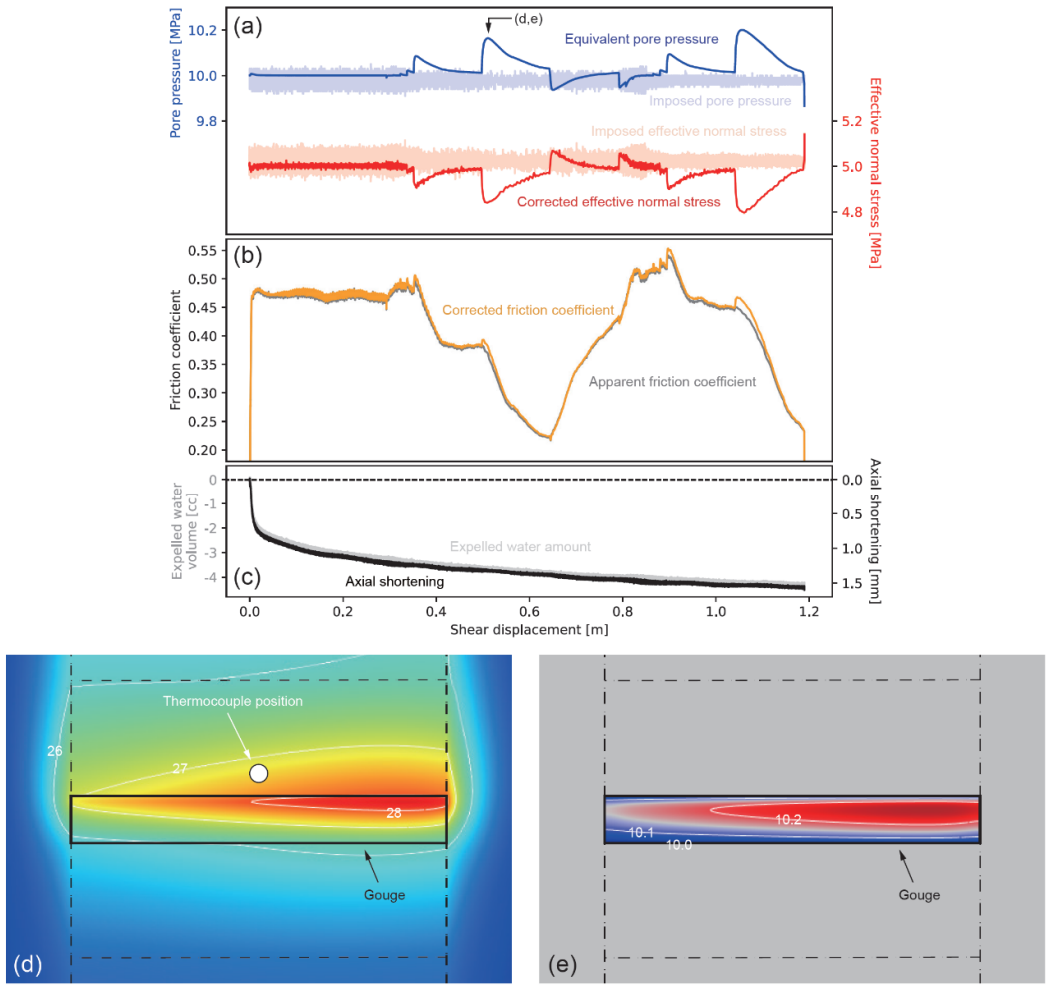

Figure 8.

Equivalent pore pressure and corrected effective normal stress conditions modeled by FEM calculations for PHV592. Permeability of 10^{-20} m^2 was assumed. (b) Apparent (gray line) and corrected friction coefficients (orange line) by the corrected effective normal stress condition. (c) Comparison between the volume of expelled water (gray line) and axial shortening (black line). Results of FEM simulation on (d) temperature and (e) pore pressure conditions at the shear displacement of ~0.5 m, indicated in (a).

406 **4. Discussion**

407 **4.1. Dynamic weakening for 100% glass caused by thermal processes**

408 The μ for 100%-glass sample at V_{eq} = 10 mm/s was higher than that typically
409 observed for quartz-rich rocks, which often shows a reduction in frictional strength at
410 similar intermediate slip velocities due to silica-gel lubrication or the formation of
411 amorphous wear materials (Goldsby & Tullis, 2002; Hayashi & Tsutsumi, 2010; Rowe
412 et al., 2019; Di Toro et al., 2004). In addition, because the dynamic weakening in the
413 100% glass sample occurred just after the maximum *T* within the gouge reached the
414 boiling *T* of 311°C for water with 10 MPa (Figure 7c), the observed dynamic weakening
415 in the multi-*V* test may be caused by vaporization of the pore water (Acosta et al., 2018;
416 Chen et al., 2017; Hunfeld et al., 2021). This result supports the idea that thermal
417 processes are important for dynamic weakening and that the amorphous grains
418 themselves do not induce the weakening (Kanagawa et al., 2020). Although the FEM
419 modeling of the single-*V* test could not estimate the *T* condition inside the gouge,
420 because the measured *T* was lower than in the multi-*V* test, the dynamic weakening in
421 the single-*V* test may instead be caused by flash heating or thermal pressurization, rather
422 than vaporization. The apparent difference in the slip distance for the dynamic
423 weakening between multi-*V* and single-*V* tests might indicate a difference in the
424 weakening mechanisms for the same materials under similar pressure conditions but
425 under different ambient *T* conditions (higher *T* for multi-*V* tests because of the frictional
426 heat generating during preceding slips); further experimental studies will be needed to
427 validate this.

428

4.2. Athermal slip weakening for low-smectite gouges at intermediate velocity range

The result of PHV592 which included both velocity upsteps and downsteps (section 3.1; Figure 4) indicated that the slip weakening behavior at the intermediate V_{eq} range (1-3 mm/s) for the 15%-smectite sample is not a result of high shear strain but purely a V dependent phenomenon. Also, the FEM modeling showed that the P_f build-up due to frictional heat had minor influence on the reduction in apparent μ values for such a low V_{eq} conditions (Figure 8). Previous studies reported similar weakening at ~1 mm/s for low-clay samples and discussed the possibility of flash heating followed by local thermal pressurization (Oohashi et al., 2013, 2015). In the case of this study, the flash heating T can be calculated by the following equation (Archard, 1959):

$$\Delta T_{flash} = \frac{1}{8}\frac{\pi \mu_a H l V_a}{K}, \#(7)$$

where V_a is the velocity at an asperity contact, and l is the size of an asperity contact, μ_a is the friction coefficient at an asperity contact, and H is the compressive yield strength of 7 GPa (Ben Abdelounis et al., 2009; Yonekura, 2015). We assume that K is 1.5 W/m/K for glass (Romine et al., 2012) and μ_a is identical to the μ value for 100% glass, i.e., μ_a = 0.6, because the asperity contact is the contact between glass grains. As the grain size in the SB was less than 30 μm (Figure 5i), we used an l value of 1-30 μm. The estimated ΔT_{flash} for V_a = 1 mm/s is 1-33°C, which is far lower than the melting T of typical rocks (~1,000°C). The ΔT_{flash} of 1-33°C may not be high enough to induce local reduction in shear strength by thermal pressurization near asperity contacts; therefore, other mechanisms would be needed to reduce frictional strength.

One possible process that could reduce μ is a fluid-like behavior of the gouge

(fluidization). For the 15%-smectite sample at intermediate V (PHV592), deformation likely occurred within the shear band (SB) with thickness of ~500 μm (Figures 6g-i) rather than a discrete shear surface like observed in the 100% glass sample with V_{eq} up to 300 mm/s (Figures 6d-f). Such distributed shear deformation is one of the characteristics of fluidization. However, further experimental and microstructural studies would be needed to ensure the occurrence of fluid-like behavior because we did not observe grain segregations, which is recognized as a form of evidence for gouge fluidization (Demurtas et al., 2021; Ujiie & Tsutsumi, 2010). In addition, because the fluidized gouge should be insensitive to σ_{eff}, we need to test the same material under different σ_{eff} conditions (Ujiie & Tsutsumi, 2010), which is planned in future work.

Another possibility is compaction-induced pore fluid pressurization. During the experiments, we observed a continuous reduction in gouge thickness which appears to depend on displacement (Figure 8c). Compaction occurred in a short time when V_{eq} was in a higher range. If we consider a simple form of P_f increase without diffusion:

$$\frac{\Delta P_f}{\Delta t} = -\frac{1}{\beta_f \, \phi \, w_g} \frac{\Delta w_g}{\Delta t}, \quad \#(8)$$

where w_g is the thickness of gouge (2 mm), and if we assume the rate of reduction in gouge thickness $\Delta w_g/\Delta t$ of 0.0025 mm/s, P_f increases by 10 MPa in a second. Therefore, the observed weakening in friction can be explained by compaction-induced pressurization, however there is a large uncertainty regarding the value of ϕ because of gouge leakage to the narrow spaces between the O-rings and Teflon liner, thus we cannot separate effects of compaction and gouge leakage on P_f. Note that compaction-induced pressurization has been reported at a high velocity conditions of ~1 m/s for the

sediment gouge from the Hikurangi subduction zone (Aretusini et al., 2021), and at a low velocity conditions of ~1 μm/s for gouges with low permeability (Faulkner et al., 2018).

4.3. Low friction coefficient at all velocity conditions for high-smectite samples

As the clay mineral content increases, the permeability of the fault gouge continuously decreases down to ~10^{-21} m^2 for 100% smectite (Takahashi et al., 2007). This low permeability contributes to the fluid overpressure within the gouge. Consequently, the frictional strength becomes quite low even at low-V conditions, such that the samples with more than 50% smectite showed low μ close to or less than 0.1 (Figure 3). Due to the intrinsic weakness of wet smectite (Morrow et al., 2017) and its impermeable nature, frictional heat generation was low and thus thermal pressurization likely did not play a significant role in the observed weakness of the clay. In addition, the chances of grain contacts among volcanic glass grains are less than low-clay samples because the volcanic glass grains are dispersed in the pervasive clay matrix and not comminuted (Figures 6k and l). This observation is consistent with the similar friction coefficients for 50%-, 70%-, and 100%-smectite samples suggesting that the smectite deformation dominantly controls the frictional behavior of the entire gouge when the clay mineral content exceeds 50% (Oohashi et al., 2013). If higher slip velocity and/or longer shear displacement were imposed, increased frictional heat would be generated, and thermal pressurization of pore fluid or water dehydrated from clay could potentially further decrease the apparent frictional strength (Hirose & Bystricky, 2007).

5. Possible impacts of slip weakening at intermediate velocity range on slow and fast earthquakes in the shallow subduction zone

The weakening with V and slip displacement can cause acceleration of fault slip and result in an earthquake. We observed V-neutral or slightly V-weakening trends up to V_{eq} = 300 μm/s for low-clay samples (see section 3.1). Considering a spring-slider model, unstable, self-accelerating slip occurs when the system stiffness K, that is the stiffness of the country rock surrounding a fault, is lower than the critical stiffness K_c, defined by frictional properties of a fault. The K_c for the (quasi-static) RSF law is described as follows:

$$K_{c,RSF} = -\frac{\sigma_{eff}(a-b)}{d_c}, \#(9)$$

where d_c is a characteristic slip distance at the V-step, and $a-b$ is defined as follows:

$$a-b = \frac{\Delta\mu_{ss}}{\Delta \ln V}, \#(10)$$

where $\Delta\mu_{ss}$ and $\Delta\ln V$ are the variation in steady-state friction coefficient and the logarithm of velocity, respectively (Dieterich, 1979; Ruina, 1983). Similarly, the K_c for a slip-weakening behavior can be defined as follows:

$$K_{c,sw} = \frac{\Delta\tau}{\delta_c}, \#(11)$$

where $\Delta\tau$ is the drop in shear stress during a characteristic slip distance δ_c (Ikari et al., 2013). The K_c value can be converted to a critical nucleation length of slip area L_c to initiate self-acceleration of slip as follows:

$$L_c = \frac{\xi G}{K_c}, \#(12)$$

512 where ξ is a shape-dependent parameter and G is the shear modulus of surrounding rock.
513 When the size of the slip length L becomes larger than L_c, then the dynamic rupture
514 initiates (Dieterich, 1992; McLaskey, 2019). For simplicity, we adopt a ξ value of $7\pi/12$
515 considering a circular crack with a diameter of L_c (Dieterich, 1986; Eshelby, 1957), and
516 a G value of 10 GPa considering partially consolidated, underthrust or accreted
517 sediment at a shallow depth in a subduction zone (e.g., S-wave velocities of 1.5-2.5
518 km/s and density of 2.0 g/cm^3 lead to 4.5-12.5 GPa) (Akuhara et al., 2020).

519 The obtained $a-b$, d_c, and calculated L_c for low V conditions, and $\Delta\tau$, δ_c, and L_c
520 for intermediate V conditions are summarized in Table 3. We used the most negative
521 $a-b$ value for each smectite content to estimate the possible unstable bound of slip. For
522 the 0%-smectite sample, V-strengthening behavior was observed for V_{eq} = 10 μm/s to
523 300 mm/s; therefore, earthquake nucleation would not be expected to occur under either
524 low or intermediate V conditions. Low-smectite samples (15-30% smectite) showed
525 negative $a-b$ values of −0.012 to −0.003 for 10 μm/s to 300 μm/s, with d_c values of
526 ~0.1 mm. At intermediate velocities, the drastic drops in shear stress $\Delta\tau$ were 1.5-0.9
527 MPa with $\delta_c \sim 0.1$ m. For high-smectite samples with more than 50% smectite, the $a-b$
528 values at the low-V conditions are almost velocity neutral (0 to 0.003). The $\Delta\tau$ values at
529 the intermediate-V condition were 0.15-0.05 MPa with $\delta_c \sim 0.1$ m.

530 The estimated L_c values for low V conditions (V_{eq} < 300 μm/s) are 30-122 m,
531 whereas those for intermediate V conditions (V_{eq} > 1 mm/s) are 1.2-36.7 km (Figure 9a,
532 Table 3). As self-accelerating slip starts when L exceeds L_c, the dependence of L_c on V
533 leads to the following two possible cases of earthquake nucleation and rupture,
534 depending on the slip length L and the slip velocity.

(case i) If L exceeds ~10-100 m (L_c for low V conditions) before the slip velocity reaches 300 μm/s, a rapid acceleration of slip initiates resulting in dynamic rupture propagation. This situation leads to the emission of seismic waves as a result of the stress drop and subsequent slip, which means a regular earthquake. It would be also possible that the slip velocity after the rupture propagation may be suppressed around intermediate V conditions when sufficient strain energy is accumulated on a fault because the shear stress of the gouge becomes minimum at the intermediate V range and fault strength cannot decrease further. Therefore, in some cases, the slip may result in a tremor that are seismologically detected slow earthquakes (Figure 9b).

(case ii) If L does not reach ~10-100 m when the slip velocity reaches 300 μm/s, a coseismic rupture does not initiate and the nucleation phase continues, because L is much smaller than L_c which becomes ~1-30 km (L_c for intermediate V conditions) and it will take a longer duration for nucleating an earthquake resulting in a slow slip event (SSE) like slip on the fault. If L exceeds ~1-30 km, then coseismic rupture will eventually occur. In the case of the Nankai subduction zone, 30 km corresponds to the entire length of the plate boundary fault beneath the outer wedge. Therefore, the coseismic rupture initiation at $L >$ ~1-30 km would generate a megathrust earthquake that ruptures all the shallow part of the plate boundary fault.

The above two cases can be interpreted to be caused by a difference in rupture velocity during the quasi-static rupture propagation: the slower the rupture velocity is, the higher the probability for a long nucleation phase becomes. This means that the large L_c for intermediate V conditions is not necessarily required for an SSE like slip. However, a larger L_c at intermediate V conditions could contribute to suppress

558 acceleration of slip and elongate the duration of nucleation phase. Therefore, the
559 weakening behavior at the intermediate V range could be an important factor that
560 controls a complex spectrum of slip behavior on a fault, although the physical
561 weakening mechanisms and constitutive law must be constrained in detail to be
562 implemented in numerical models. Since the transition from volcanic glass to smectite
563 occurs in the shallow part of subduction zones, and as the smectite content increases
564 with depth, the plate boundary fault would gradually be more likely to host slow
565 earthquakes, as observed in the Nankai Trough where slow earthquakes have been
566 observed beneath the accretionary prism (Figure 9c). At deeper depths where smectite
567 dehydrates into illite at $T \sim 150$℃ or σ_{eff} will become high, frictional properties may
568 change, or L_c will decrease, which will make the plate boundary fault more prone to
569 regular earthquakes.
570

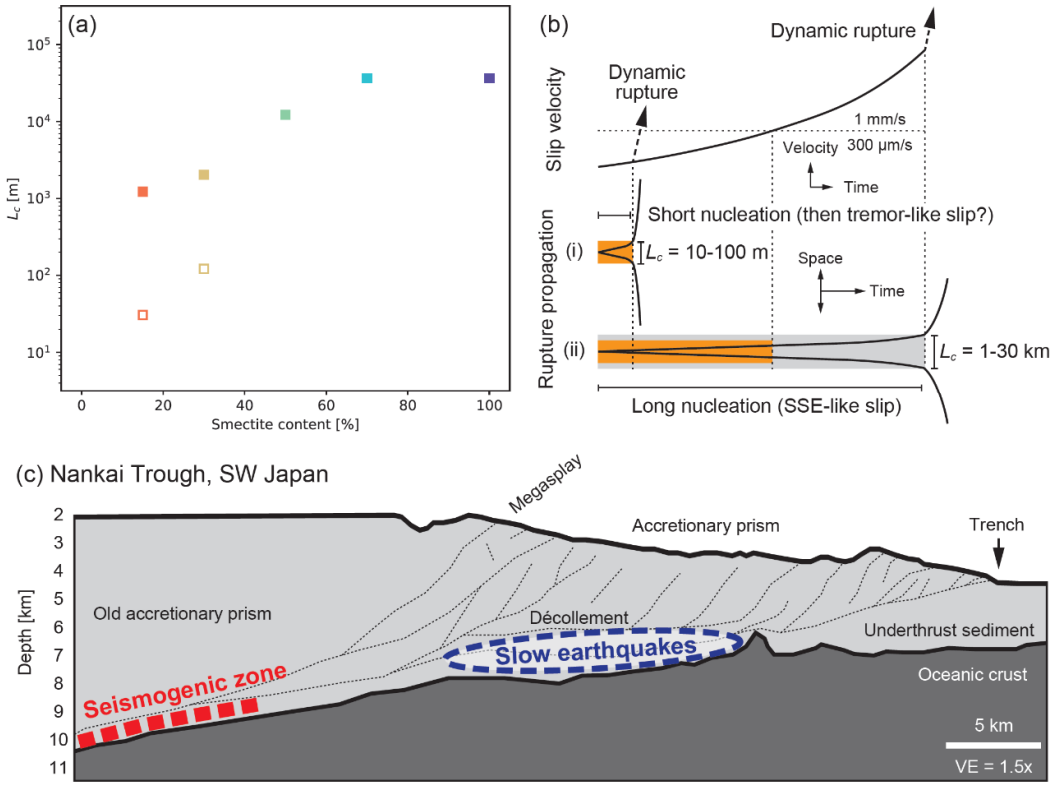

571

572 **Figure 9.**

573 (a) The L_c values for different smectite contents with low velocity range (open square)
574 and intermediate velocity range (filled square). The d_c values are assumed to be 1 mm
575 for low velocity range and 0.1 m for intermediate velocity range. (b) Schematic
576 illustration for the evolutions of slip velocity that can generate slow earthquakes (see
577 text for details). Orange and gray areas represent the critical nucleation length L_c for low
578 and intermediate velocity conditions, respectively. (c) A sketch of the cross section of
579 the Nankai Trough, SW Japan (Moore et al., 2009) overlaid by locations of slow
580 earthquakes and the seismogenic zone.

581

582 **Table 3.**

583 Summary of velocity dependence at low and intermediate velocity conditions. All
584 parameters are the case for the effective normal stress of 5 MPa. "X" means that L_c
585 cannot be defined because $a-b$ is positive.

	Low V conditions (RSF)			Intermediate V conditions (slip weakening)		
	$(a-b)\sigma_{eff}$	d_c	L_c	$\Delta\tau$	δ_c	L_c
Glass/Smectite = 100/0	0.075 MPa	~0.1 mm	X	0.25 MPa	~0.1 mm	X
Glass/Smectite = 85/15	-0.06 MPa	~0.1 mm	30 m	-1.5 MPa	~0.1 m	1.2 km
Glass/Smectite = 70/30	-0.015 MPa	~0.1 mm	122 m	-0.9 MPa	~0.1 m	2.0 km
Glass/Smectite = 50/50	0.015 MPa	~0.1 mm	X	-0.15 MPa	~0.1 m	12.2 km
Glass/Smectite = 30/70	0 MPa	~0.1 mm	X	-0.05 MPa	~0.1 m	36.7 km
Glass/Smectite = 0/100	0 MPa	~0.1 mm	X	-0.05 MPa	~0.1 m	36.7 km

586

587 **6. Conclusions**

588 We performed a series of friction experiments on a range of volcanic glass
589 smectite mixtures at different velocity conditions. For low-velocity conditions (<1
590 mm/s), friction coefficients decreased with increased smectite content. Samples with 15

591 and 30% smectite characteristically showed a negative velocity dependence of friction
592 coefficients. At intermediate-velocity conditions (1-3 mm/s), samples with 15 and 30%
593 smectite showed marked slip-weakening behavior with a characteristic slip distance of
594 ~0.1 m. At high-velocity conditions (>100 mm/s), the volcanic glass exhibited dynamic
595 weakening behavior caused by thermal processes such as vaporization. Silica-gel
596 lubrication likely does not explain the observed dynamic weakening behavior. Although
597 the underlying physical processes are still undetermined, the marked weakening
598 behavior at intermediate velocity conditions will produce large critical nucleation
599 lengths on the order of 1-30 km. Such weakening behavior at intermediate velocity
600 conditions potentially induces slow earthquakes, as observed in shallow subduction
601 zones such as the Nankai Trough.
602
603 **Appendix A: Derivation of equivalent pore pressure**
604 To define the equivalent pore pressure P_{feq} (equation 5), we consider the total
605 work for shear deformation similar to the derivation of equivalent velocity V_{eq}
606 (Shimamoto & Tsutsumi, 1994). Assuming μ does not depend on r, the shear stress at r
607 can be written as:

$$\tau(r) = \mu_{obs}(\sigma_n - P_{fo}) = \mu_{cor}\left(\sigma_n - P_f(r)\right). \#(A1)$$

608 The work for shear deformation at r can be described as:

$$dw = V(r)\tau(r)(2\pi r)dr = \frac{3}{4}V_{eq}(2r)\frac{r_o + r_i}{r_o^2 + r_o r_i + r_i^2}\tau(r)(2\pi r)dr, \#(A2)$$

609 and thus the total work on the entire shear plane is:

$$W = \int_{r_i}^{r_o} dw = \int_{r_i}^{r_o} C\, r^2 \tau(r)dr, \#(A3)$$

where

$$C = 3\pi V_{eq}\frac{r_o + r_i}{r_o^2 + r_o r_i + r_i^2}. \#(A4)$$

Since equation A3 can be converted as follows:

$$W = \int_{r_i}^{r_o} C\, r^2 \mu_{obs}(\sigma_n - P_{fo})dr = \int_{r_i}^{r_o} C\, r^2 \mu_{cor}\left(\sigma_n - P_f(r)\right)dr, \#(A5)$$

we obtain the following equation:

$$\mu_{obs}(\sigma_n - P_{fo})\frac{r_o^3 - r_i^3}{3} = \mu_{cor}\left(\sigma_n \frac{r_o^3 - r_i^3}{3} - \int_{r_i}^{r_o} P_f(r) r^2 dr\right). \#(A6)$$

Considering the average P_f within the shear localized zone with the thickness w_{hs}, we can describe $P_f(r)$ as follows:

$$P_f(r) = \int_{z_{hs}^{bot}}^{z_{hs}^{top}} \frac{P_f(r,z)}{w_{hs}} dz. \#(A7)$$

If we define P_{feq} as follows:

$$P_{feq} = \frac{3}{r_o^3 - r_i^3}\int_{r_i}^{r_o} P_f(r) r^2\, dr = \frac{3}{r_o^3 - r_i^3}\int_{r_i}^{r_o}\int_{z_{hs}^{bot}}^{z_{hs}^{top}} \frac{P_f(r,z) r^2}{w_{hs}} dz\, dr, \#(A8)$$

equation A6 can be converted to:

$$\mu_{obs}(\sigma_n - P_{fo}) = \mu_{cor}(\sigma_n - P_{feq}). \#(A9)$$

Therefore, P_{feq} represents the "equivalent" pore pressure for radially heterogenous pore pressure condition, which can be considered as the representative P_f value in the shear localized zone.

Acknowledgements

We thank John Bedford (JAMSTEC) for discussion, Takahiro Suzuki and Osamu Tadai

(Marine Works Japan Ltd.) for technical assistance during experiments, Ryo Nakanishi, Yuichi Okuma, and Ippei Yamamoto (AORI, Univ. Tokyo) for sample preparations, Nobuhiro Ogawa (AORI, Univ. Tokyo) for SEM analyses, and Manami Kitamura (GSJ, AIST) for FEM modeling. This work is supported by KAKENHI grants (JP20J20413 and JP16K21728 to H. Okuda, JP20F20786 and JP22H05319 to T. Hirose, JP19H04621, JP21H01189, and JP21H05202 to A. Yamaguchi). H. Okuda is supported by DC1 fellowship from Japan Society for the Promotion of Science (JSPS).

Open research

The experimental data can be available from https://doi.org/10.17632/587wnsdgdb.1.

References

Ben Abdelounis, H., Elleuch, K., Vargiolu, R., Zahouani, H., & Le Bot, A. (2009). On the behaviour of obsidian under scratch test. *Wear*, *266*(7–8), 621–626. https://doi.org/10.1016/j.wear.2008.07.007

Acosta, M., Passelegue, F., Schubnel, A., & Violay, M. (2018). Dynamic weakening during earthquakes controlled by fluid thermodynamics. *Nature Communications*, *9*(1), 3074. https://doi.org/10.1038/s41467-018-05603-9

Akuhara, T., Tsuji, T., & Tonegawa, T. (2020). Overpressured Underthrust Sediment in the Nankai Trough Forearc Inferred From Transdimensional Inversion of High-Frequency Teleseismic Waveforms. *Geophysical Research Letters*, *47*(15). https://doi.org/10.1029/2020GL088280

Archard, J. F. (1959). The temperature of rubbing surfaces. *Wear*, *2*(6), 438–455.

https://doi.org/10.1016/0043-1648(59)90159-0

Aretusini, S., Meneghini, F., Spagnuolo, E., Harbord, C. W. A., & Di Toro, G. (2021). Fluid pressurisation and earthquake propagation in the Hikurangi subduction zone. *Nature Communications*, *12*(1), 2481. https://doi.org/10.1038/s41467-021-22805-w

Bedford, J. D., Faulkner, D. R., & Lapusta, N. (2022). Fault rock heterogeneity can produce fault weakness and reduce fault stability. *Nature Communications*, *13*(1), 326. https://doi.org/10.1038/s41467-022-27998-2

Byerlee, J. D. (1978). Friction of rocks. *Pure and Applied Geophysics PAGEOPH*, *116*(4–5), 615–626. https://doi.org/10.1007/BF00876528

Chen, J., Niemeijer, A., Yao, L., & Ma, S. (2017). Water vaporization promotes coseismic fluid pressurization and buffers temperature rise. *Geophysical Research Letters*, *44*(5), 2177–2185. https://doi.org/10.1002/2016GL071932

Chester, F. M., Rowe, C. D., Ujiie, K., Kirkpatrick, J. D., Regalla, C., Remitti, F., et al. (2013). Structure and Composition of the Plate-Boundary Slip Zone for the 2011 Tohoku-Oki Earthquake. *Science*, *342*(6163), 1208–1211. https://doi.org/10.1126/science.1243719

Compton, J. S. (1991). Origin and Diagenesis of Clay Minerals in the Monterey Formation, Santa Maria Basin Area, California. *Clays and Clay Minerals*, *39*(5), 449–466. https://doi.org/10.1346/CCMN.1991.0390501

Dieterich, J. H. (1979). Modeling of rock friction: 1. Experimental results and constitutive equations. *Journal of Geophysical Research*, *84*(B5), 2161. https://doi.org/10.1029/JB084iB05p02161

669 Faulkner, D. R., Mitchell, T. M., Behnsen, J., Hirose, T., & Shimamoto, T. (2011).
670 Stuck in the mud? Earthquake nucleation and propagation through accretionary
671 forearcs. *Geophysical Research Letters*, *38*(18), n/a-n/a.
672 https://doi.org/10.1029/2011GL048552
673 Faulkner, D. R., Sánchez-Roa, C., Boulton, C., den Hartog, S. A. M., Sanchez-Roa, C.,
674 Boulton, C., & den Hartog, S. A. M. (2018). Pore Fluid Pressure Development in
675 Compacting Fault Gouge in Theory, Experiments, and Nature. *Journal of*
676 *Geophysical Research: Solid Earth*, *123*(1), 226–241.
677 https://doi.org/10.1002/2017JB015130
678 Goldsby, D. L., & Tullis, T. E. (2002). Low frictional strength of quartz rocks at
679 subseismic slip rates. *Geophysical Research Letters*, *29*(17), 1844.
680 https://doi.org/10.1029/2002GL015240
681 Han, R., Kim, J.-S., Kim, C.-M., Hirose, T., Jeong, J. O., & Jeong, G. Y. (2019).
682 Dynamic weakening of ring faults and catastrophic caldera collapses. *Geology*,
683 *47*(2), 107–110. https://doi.org/10.1130/G45687.1
684 Harders, R., Kutterolf, S., Hensen, C., Moerz, T., & Brueckmann, W. (2010). Tephra
685 layers: A controlling factor on submarine translational sliding? *Geochemistry,*
686 *Geophysics, Geosystems*, *11*(5), n/a-n/a. https://doi.org/10.1029/2009GC002844
687 Hayashi, N., & Tsutsumi, A. (2010). Deformation textures and mechanical behavior of
688 a hydrated amorphous silica formed along an experimentally produced fault in
689 chert. *Geophysical Research Letters*, *37*(12), n/a-n/a.
690 https://doi.org/10.1029/2010GL042943
691 Hirose, T., & Bystricky, M. (2007). Extreme dynamic weakening of faults during

692 dehydration by coseismic shear heating. *Geophysical Research Letters*, *34*(14),
693 L14311. https://doi.org/10.1029/2007GL030049
694 Hunfeld, L. B., Chen, J., Niemeijer, A. R., Ma, S., & Spiers, C. J. (2021). Seismic Slip-
695 Pulse Experiments Simulate Induced Earthquake Rupture in the Groningen Gas
696 Field. *Geophysical Research Letters*, *48*(11).
697 https://doi.org/10.1029/2021GL092417
698 Ikari, M. J., Marone, C., Saffer, D. M., & Kopf, A. J. (2013). Slip weakening as a
699 mechanism for slow earthquakes. *Nature Geoscience*, *6*(6), 468–472.
700 https://doi.org/10.1038/ngeo1818
701 Ikari, M. J., Kopf, A. J., Hüpers, A., & Vogt, C. (2018). Lithologic control of frictional
702 strength variations in subduction zone sediment inputs. *Geosphere*, *14*(2), 604–625.
703 https://doi.org/10.1130/GES01546.1
704 Kameda, J., Shimizu, M., Ujiie, K., Hirose, T., Ikari, M. J., Mori, J. J., et al. (2015).
705 Pelagic smectite as an important factor in tsunamigenic slip along the Japan Trench.
706 *Geology*, *43*(2), 155–158. https://doi.org/10.1130/G35948.1
707 Kanagawa, K., Murayama, H., Sugita, A., Takahashi, M., Sawai, M., Furukawa, N., &
708 Hirose, T. (2020). Weakening of quartz rocks at subseismic slip rates due to
709 frictional heating, but not to lubrication by wear materials of hydrated amorphous
710 silica or silica gel. *Tectonophysics*, *784*(April 2019), 228429.
711 https://doi.org/10.1016/j.tecto.2020.228429
712 Kluger, M. O., Jorat, M. E., Moon, V. G., Kreiter, S., de Lange, W. P., Mörz, T., et al.
713 (2020). Rainfall threshold for initiating effective stress decrease and failure in
714 weathered tephra slopes. *Landslides*, *17*(2), 267–281.

https://doi.org/10.1007/s10346-019-01289-2

Laberg, J. S., Strasser, M., Alves, T. M., Gao, S., Kawamura, K., Kopf, A. J., & Moore, G. F. (2017). Internal deformation of a muddy gravity flow and its interaction with the seafloor (site C0018 of IODP Expedition 333, Nankai Trough, SE Japan). *Landslides*, *14*(3), 849–860. https://doi.org/10.1007/s10346-016-0766-7

Lavallée, Y., Hirose, T., Kendrick, J. E., De Angelis, S., Petrakova, L., Hornby, A. J., & Dingwell, D. B. (2014). A frictional law for volcanic ash gouge. *Earth and Planetary Science Letters*, *400*, 177–183. https://doi.org/10.1016/j.epsl.2014.05.023

Logan, J. M., & Rauenzahn, K. A. (1987). Frictional dependence of gouge mixtures of quartz and montmorillonite on velocity, composition and fabric. *Tectonophysics*, *144*(1–3), 87–108. https://doi.org/10.1016/0040-1951(87)90010-2

Moon, V. (2016). Halloysite behaving badly: geomechanics and slope behaviour of halloysite-rich soils. *Clay Minerals*, *51*(3), 517–528. https://doi.org/10.1180/claymin.2016.051.3.09

Morrow, C. A., Moore, D. E., & Lockner, D. A. (2017). Frictional strength of wet and dry montmorillonite. *Journal of Geophysical Research: Solid Earth*, *122*(5), 3392–3409. https://doi.org/10.1002/2016JB013658

Nakamura, S., Wakai, A., Umemura, J., Sugimoto, H., & Takeshi, T. (2014). Earthquake-induced landslides: Distribution, motion and mechanisms. *Soils and Foundations*, *54*(4), 544–559. https://doi.org/10.1016/j.sandf.2014.06.001

Nakamura, Y. (2016). Stratigraphy, distribution, and petrographic properties of Holocene tephras in Hokkaido, northern Japan. *Quaternary International*, *397*, 52–

62. https://doi.org/10.1016/j.quaint.2015.07.056

Nakanishi, R., Ashi, J., & Okamura, S. (2020). A dataset for distribution and characteristics of Holocene pyroclastic fall deposits along the Pacific coasts in western Hokkaido, Japan. *Data in Brief*, *33*, 106565. https://doi.org/10.1016/j.dib.2020.106565

Okuda, H., Ikari, M. J., Roesner, A., Stanislowski, K., Hüpers, A., Yamaguchi, A., & Kopf, A. J. (2021). Spatial Patterns in Frictional Behavior of Sediments Along the Kumano Transect in the Nankai Trough. *Journal of Geophysical Research: Solid Earth*, *126*(11). https://doi.org/10.1029/2021JB022546

Oohashi, K., Hirose, T., & Shimamoto, T. (2013). Graphite as a lubricating agent in fault zones: An insight from low- to high-velocity friction experiments on a mixed graphite-quartz gouge. *Journal of Geophysical Research: Solid Earth*, *118*(5), 2067–2084. https://doi.org/10.1002/jgrb.50175

Oohashi, K., Hirose, T., Takahashi, M., & Tanikawa, W. (2015). Dynamic weakening of smectite-bearing faults at intermediate velocities: Implications for subduction zone earthquakes. *Journal of Geophysical Research: Solid Earth*, *120*(3), 1572–1586. https://doi.org/10.1002/2015JB011881

Rempe, M., Smith, S. A. F., Mitchell, T. M., Hirose, T., & Di Toro, G. (2017). The effect of water on strain localization in calcite fault gouge sheared at seismic slip rates. *Journal of Structural Geology*, *97*, 104–117. https://doi.org/10.1016/j.jsg.2017.02.007

Rice, J. R. (2006). Heating and weakening of faults during earthquake slip. *Journal of Geophysical Research: Solid Earth*, *111*(B5), n/a-n/a.

https://doi.org/10.1029/2005JB004006

Romine, W. L., Whittington, A. G., Nabelek, P. I., & Hofmeister, A. M. (2012). Thermal diffusivity of rhyolitic glasses and melts: effects of temperature, crystals and dissolved water. *Bulletin of Volcanology*, *74*(10), 2273–2287. https://doi.org/10.1007/s00445-012-0661-6

Rowe, C. D., Lamothe, K., Rempe, M., Andrews, M., Mitchell, T. M., Di Toro, G., et al. (2019). Earthquake lubrication and healing explained by amorphous nanosilica. *Nature Communications*, *10*(1), 1–11. https://doi.org/10.1038/s41467-018-08238-y

Ruina, A. L. (1983). Slip instability and state variable friction laws. *Journal of Geophysical Research: Solid Earth*, *88*(B12), 10359–10370. https://doi.org/10.1029/JB088iB12p10359

Screaton, E. J., Kimura, G., Curewitz, D., Moore, G. F., Chester, F. M., Fabbri, O., et al. (2009). Interactions between deformation and fluids in the frontal thrust region of the NanTroSEIZE transect offshore the Kii Peninsula, Japan: Results from IODP Expedition 316 Sites C0006 and C0007. *Geochemistry, Geophysics, Geosystems*, *10*(12), n/a-n/a. https://doi.org/10.1029/2009GC002713

Scudder, R. P., Murray, R. W., Kutterolf, S., Schindlbeck, J. C., Underwood, M. B., & Wang, K.-L. (2018). Sedimentary inputs to the Nankai subduction zone: The importance of dispersed ash. *Geosphere*, *14*(4), 1451–1467. https://doi.org/10.1130/GES01558.1

Shimamoto, T., & Tsutsumi, A. (1994). A new rotary-shear high-speed frictional testing machine: its basic design and scope of research. *Journal of the Tectonic Research Group, Japan*. Retrieved from https://ci.nii.ac.jp/naid/80008741644/

784 Shimizu, O., & Ono, M. (2016). Relationship of tephra stratigraphy and hydraulic
785 conductivity with slide depth in rainfall-induced shallow landslides in Aso
786 Volcano, Japan. *Landslides*, *13*(3), 577–582. https://doi.org/10.1007/s10346-015-
787 0666-2
788 Strasser, M., Henry, P., Kanamatsu, T., Thu, M. K., & Moore, G. F. (2012). Scientific
789 Drilling of Mass-Transport Deposits in the Nankai Accretionary Wedge: First
790 Results from IODP Expedition 333. In *Submarine Mass Movements and Their*
791 *Consequences* (pp. 671–681). Dordrecht: Springer Netherlands.
792 https://doi.org/10.1007/978-94-007-2162-3_60
793 Takahashi, M., Mizoguchi, K., Kitamura, K., & Masuda, K. (2007). Effects of clay
794 content on the frictional strength and fluid transport property of faults. *Journal of*
795 *Geophysical Research*, *112*(B8), B08206. https://doi.org/10.1029/2006JB004678
796 Tanikawa, W., Mukoyoshi, H., Tadai, O., Hirose, T., Tsutsumi, A., & Lin, W. (2012).
797 Velocity dependence of shear-induced permeability associated with frictional
798 behavior in fault zones of the Nankai subduction zone. *Journal of Geophysical*
799 *Research: Solid Earth*, *117*(5), 1–16. https://doi.org/10.1029/2011JB008956
800 Tanikawa, W., Ishikawa, T., Honda, G., Hirono, T., & Tadai, O. (2015). Trace element
801 anomaly in fault rock induced by coseismic hydrothermal reactions reproduced in
802 laboratory friction experiments. *Geophysical Research Letters*, *42*(9), 3210–3217.
803 https://doi.org/10.1002/2015GL063195
804 Tembe, S., Lockner, D. A., & Wong, T.-F. (2010). Effect of clay content and
805 mineralogy on frictional sliding behavior of simulated gouges: Binary and ternary
806 mixtures of quartz, illite, and montmorillonite. *Journal of Geophysical Research*,

807 *115*(B3), B03416. https://doi.org/10.1029/2009JB006383
808 Di Toro, G., Goldsby, D. L., & Tullis, T. E. (2004). Friction falls towards zero in quartz
809 rock as slip velocity approaches seismic rates. *Nature*, *427*(6973), 436–439.
810 https://doi.org/10.1038/nature02249
811 Ujiie, K., & Tsutsumi, A. (2010). High-velocity frictional properties of clay-rich fault
812 gouge in a megasplay fault zone, Nankai subduction zone. *Geophysical Research*
813 *Letters*, *37*(24), L24310. https://doi.org/10.1029/2010GL046002
814 Ujiie, K., Tanaka, H., Saito, T., Tsutsumi, A., Mori, J. J., Kameda, J., et al. (2013). Low
815 Coseismic Shear Stress on the Tohoku-Oki Megathrust Determined from
816 Laboratory Experiments. *Science*, *342*(6163), 1211–1214.
817 https://doi.org/10.1126/science.1243485
818 Wiemer, G., & Kopf, A. J. (2015). Altered marine tephra deposits as potential slope
819 failure planes? *Geo-Marine Letters*, *35*(4), 305–314.
820 https://doi.org/10.1007/s00367-015-0408-4
821 Wiemer, G., & Kopf, A. J. (2017). On the role of volcanic ash deposits as preferential
822 submarine slope failure planes. *Landslides*, *14*(1), 223–232.
823 https://doi.org/10.1007/s10346-016-0706-6
824 Wiemer, G., Moernaut, J., Stark, N., Kempf, P., De Batist, M., Pino, M., et al. (2015).
825 The role of sediment composition and behavior under dynamic loading conditions
826 on slope failure initiation: a study of a subaqueous landslide in earthquake-prone
827 South-Central Chile. *International Journal of Earth Sciences*, *104*(5), 1439–1457.
828 https://doi.org/10.1007/s00531-015-1144-8
829 Yonekura, K. (2015). Rock properties and material selection for blade manufacture in

upper paleolithic Japan. *Lithic Technology*, *40*(2), 85–93.
https://doi.org/10.1179/2051618515Y.0000000001

Figure 1.

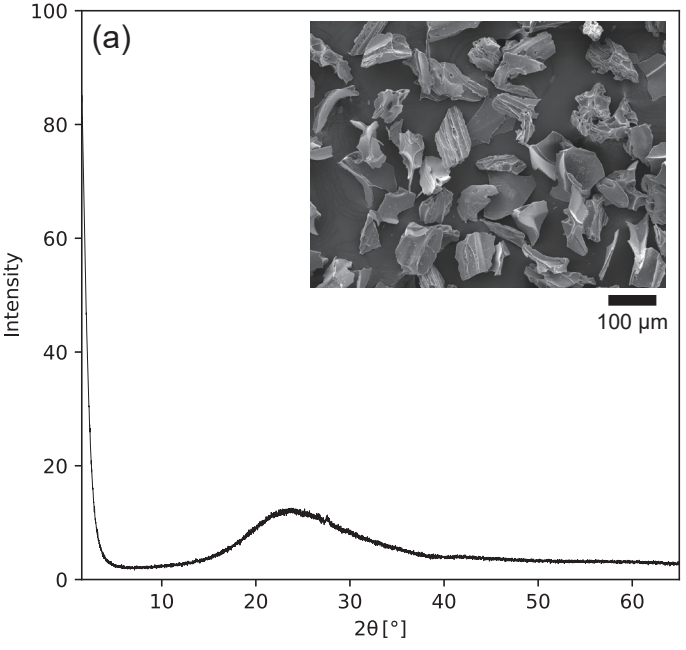
(a)
100 µm
Intensity
2θ[°]

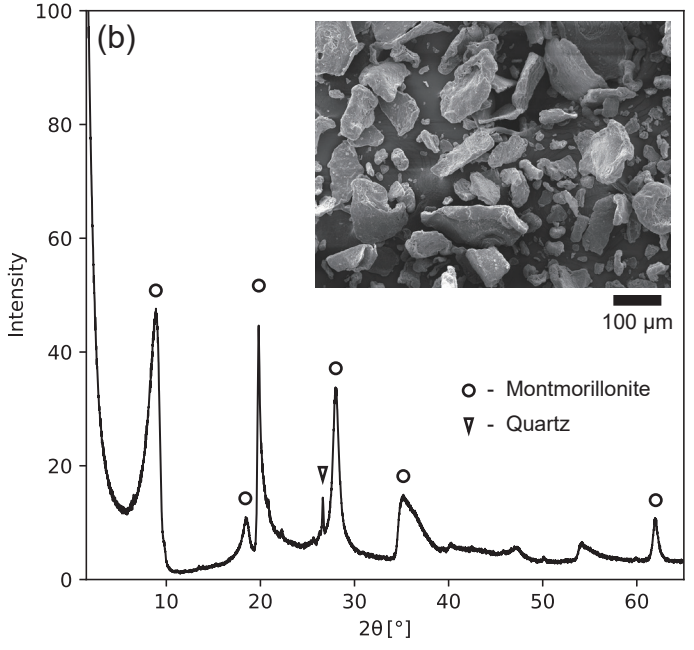
(b)
100 µm
Intensity
2θ[°]
- Montmorillonite
- Quartz


(c) Smectite 0%
100 µm


(d) Smectite 15%
100 µm

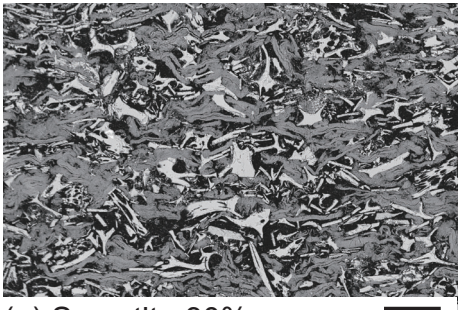
(e) Smectite 30%
100 µm

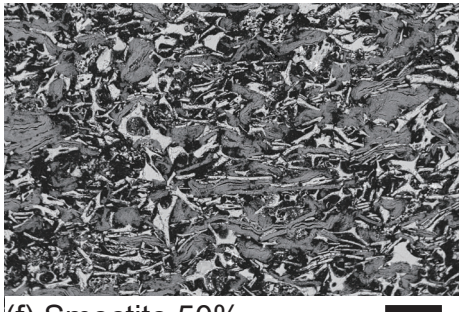
(f) Smectite 50%
100 µm

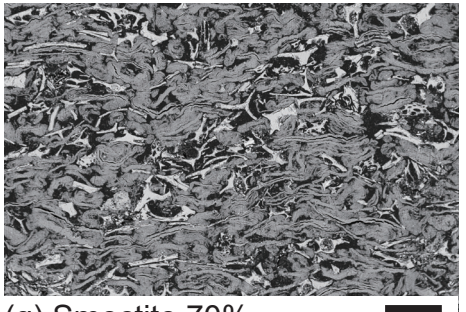
(g) Smectite 70%
100 µm

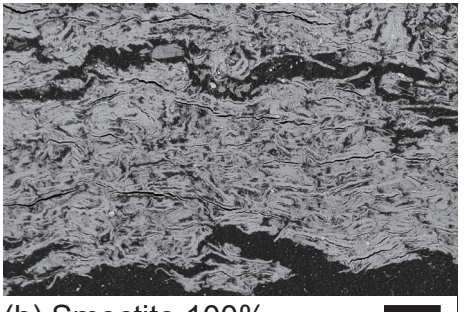
(h) Smectite 100%
100 µm

Figure 2.

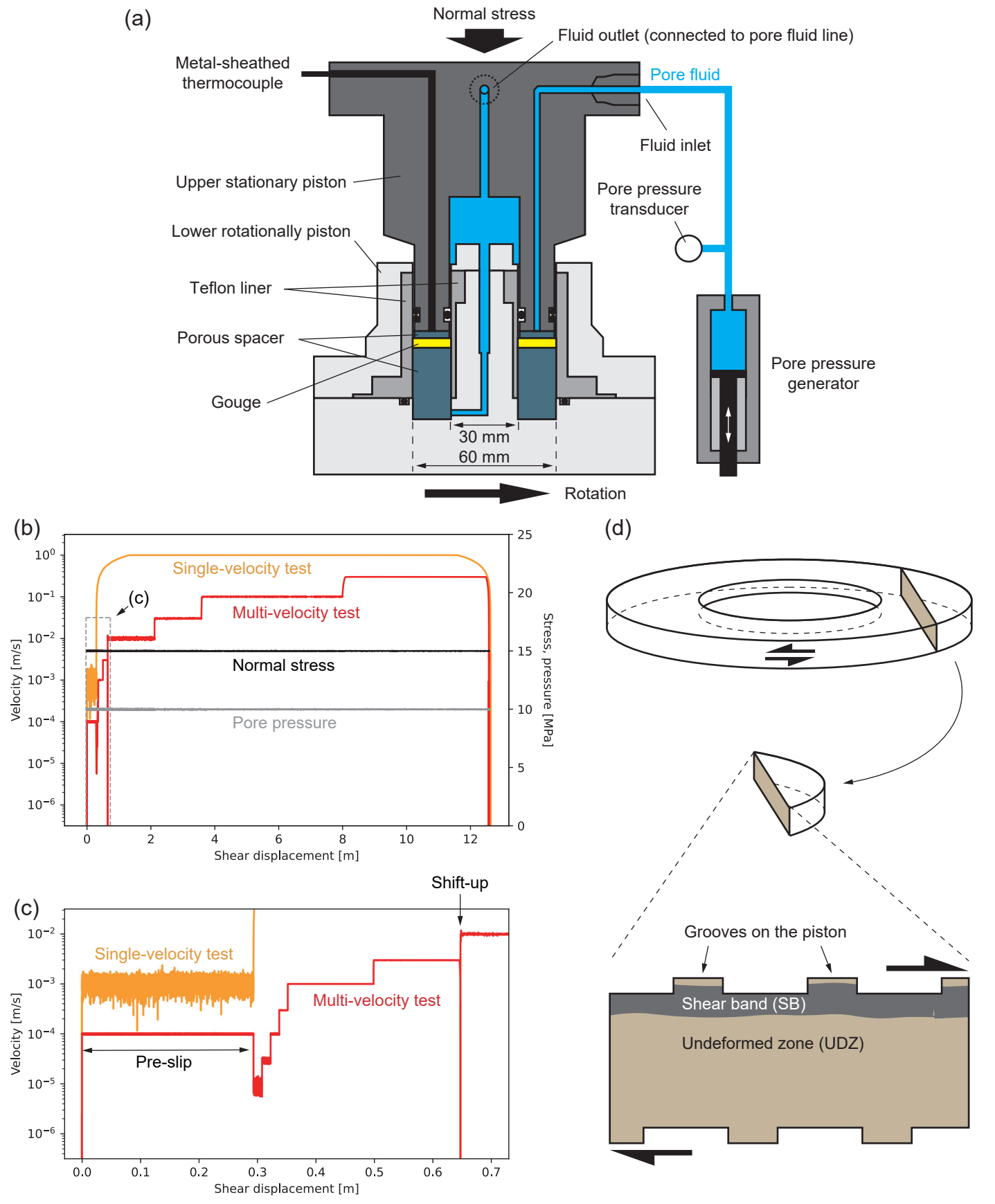
(a)
Normal stress
Fluid outlet (connected to pore fluid line)
Metal-sheathed thermocouple
Pore fluid
Fluid inlet
Upper stationary piston
Pore pressure transducer
Lower rotationally piston
Teflon liner
Porous spacer
Gouge
Pore pressure generator
30 mm
60 mm
Rotation
(b)
Single-velocity test
(c)
Multi-velocity test
Normal stress
Pore pressure
Velocity [m/s]
Stress, pressure [MPa]
Shear displacement [m]
(c)
Shift-up
Single-velocity test
Multi-velocity test
Pre-slip
Velocity [m/s]
Shear displacement [m]
(d)
Grooves on the piston
Shear band (SB)
Undeformed zone (UDZ)

Figure 3.

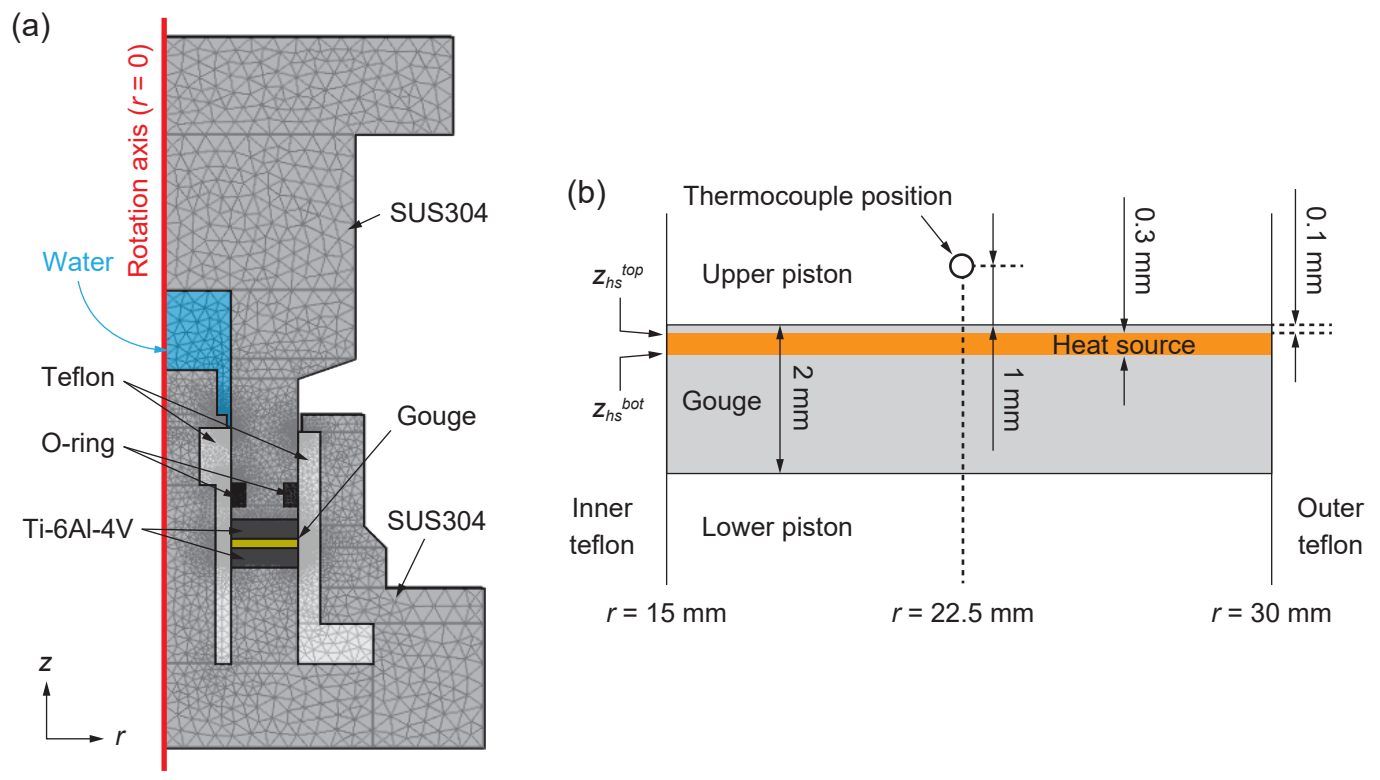
(a)
Rotation axis (r = 0)
SUS304
Water
Teflon
O-ring
Gouge
Ti-6Al-4V
SUS304
z
r
(b)
Thermocouple position
0.3 mm
0.1 mm
z_{hs}^{top}
Upper piston
Heat source
z_{hs}^{bot}
Gouge
2 mm
1 mm
Inner teflon
Lower piston
Outer teflon
r = 15 mm
r = 22.5 mm
r = 30 mm

Figure 4.

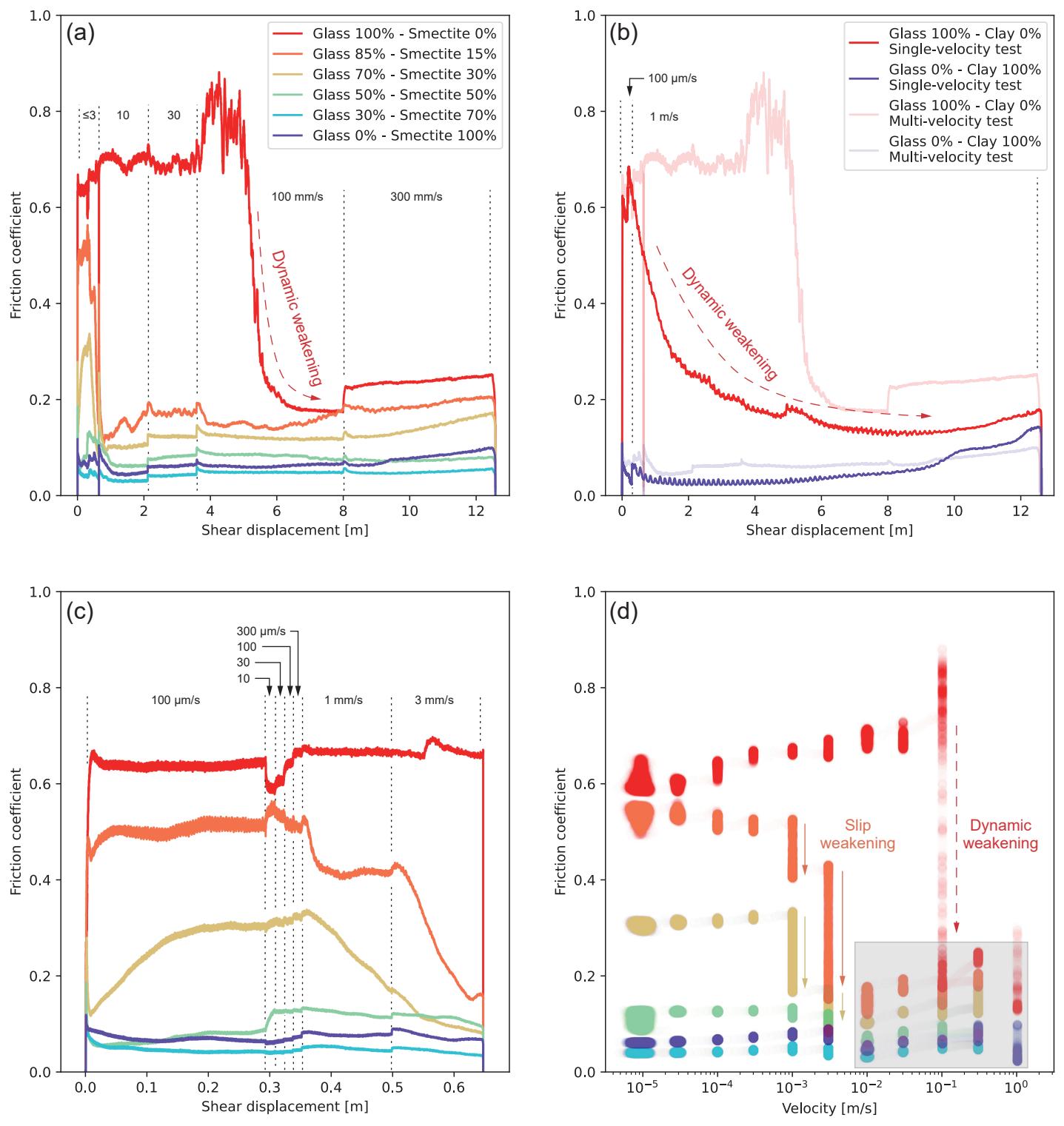
(a)
Glass 100% - Smectite 0%
Glass 85% - Smectite 15%
Glass 70% - Smectite 30%
Glass 50% - Smectite 50%
Glass 30% - Smectite 70%
Glass 0% - Smectite 100%
≤3
10
30
100 mm/s
300 mm/s
Dynamic weakening
Friction coefficient
Shear displacement [m]
(b)
Glass 100% - Clay 0%
Single-velocity test
Glass 0% - Clay 100%
Single-velocity test
Glass 100% - Clay 0%
Multi-velocity test
Glass 0% - Clay 100%
Multi-velocity test
100 µm/s
1 m/s
Dynamic weakening
Friction coefficient
Shear displacement [m]
(c)
300 µm/s
100
30
10
100 µm/s
1 mm/s
3 mm/s
Friction coefficient
Shear displacement [m]
(d)
Slip weakening
Dynamic weakening
Friction coefficient
Velocity [m/s]

Figure 5.

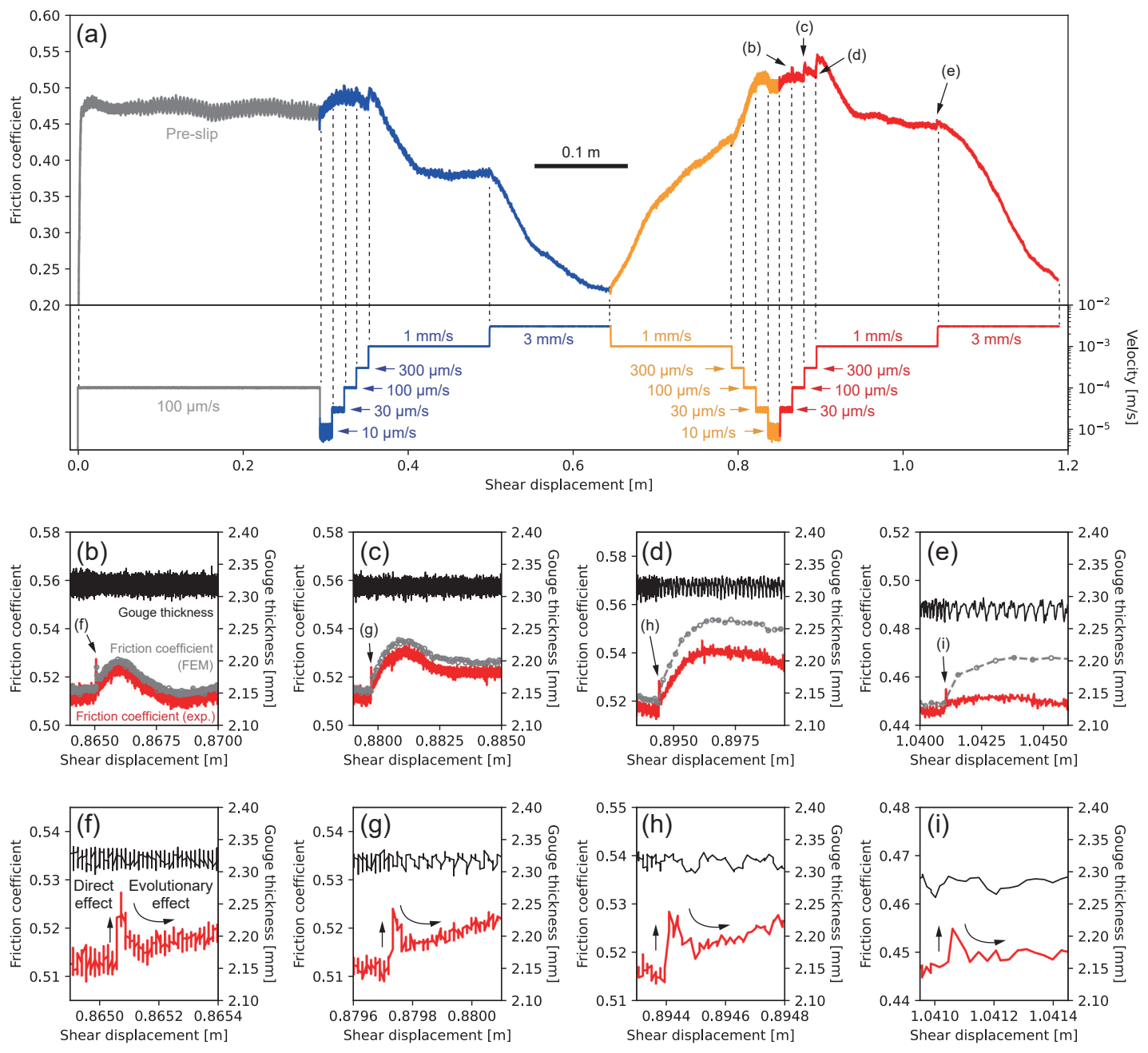
(a)
Friction coefficient
Pre-slip
0.1 m
(b)
(c)
(d)
(e)
1 mm/s
3 mm/s
300 μm/s
100 μm/s
30 μm/s
10 μm/s
100 μm/s
Velocity [m/s]
Shear displacement [m]
(b)
(c)
(d)
(e)
Gouge thickness
Friction coefficient (FEM)
Friction coefficient (exp.)
(f)
(g)
(h)
(i)
Friction coefficient
Gouge thickness [mm]
Shear displacement [m]
(f)
(g)
(h)
(i)
Direct effect
Evolutionary effect

Figure 6.

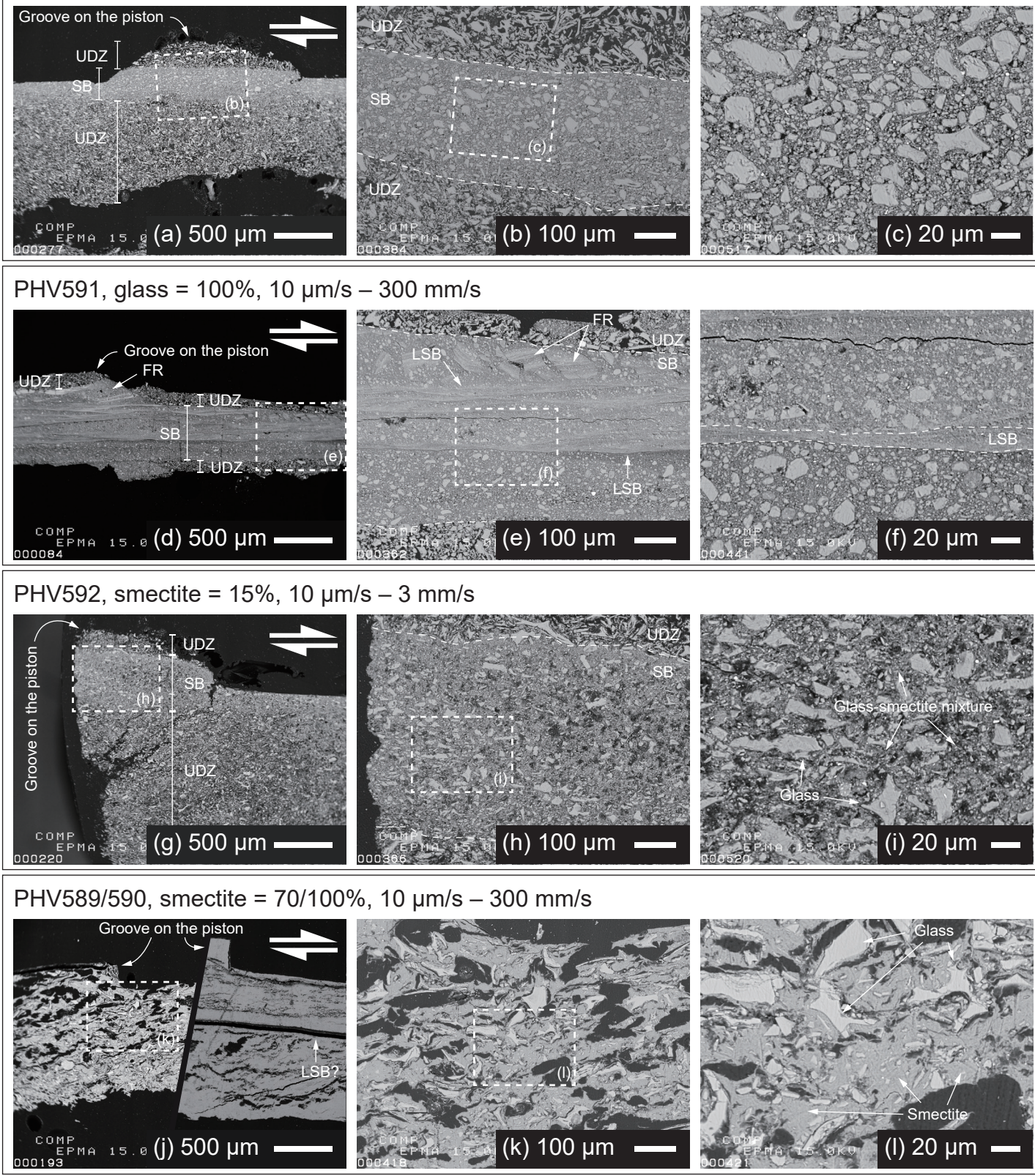
PHV596, glass = 100%, 10 µm/s – 3 mm/s
Groove on the piston
UDZ
SB
UDZ
(b)
(a) 500 µm
UDZ
SB
(c)
UDZ
(b) 100 µm
(c) 20 µm
PHV591, glass = 100%, 10 µm/s – 300 mm/s
Groove on the piston
FR
UDZ
UDZ
SB
UDZ
(e)
(d) 500 µm
FR
UDZ
LSB
SB
(f)
LSB
(e) 100 µm
LSB
(f) 20 µm
PHV592, smectite = 15%, 10 µm/s – 3 mm/s
Groove on the piston
UDZ
SB
(h)
UDZ
(g) 500 µm
UDZ
SB
(i)
(h) 100 µm
Glass-smectite mixture
Glass
(i) 20 µm
PHV589/590, smectite = 70/100%, 10 µm/s – 300 mm/s
Groove on the piston
(k)
LSB?
(j) 500 µm
(l)
(k) 100 µm
Glass
Smectite
(l) 20 µm

Figure 7.

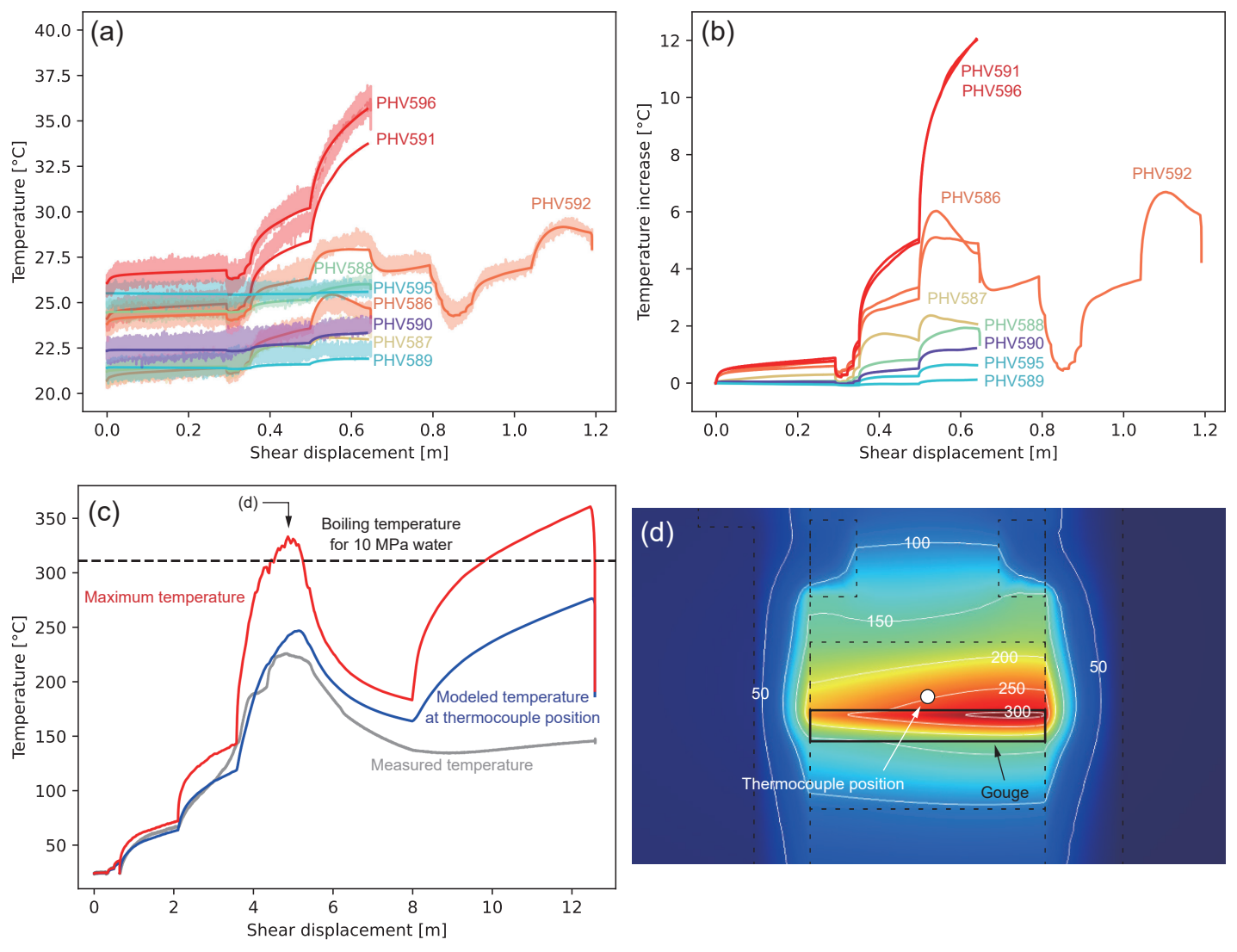
(a)
Temperature [°C]
Shear displacement [m]
PHV596
PHV591
PHV592
PHV588
PHV595
PHV586
PHV590
PHV587
PHV589
(b)
Temperature increase [°C]
Shear displacement [m]
PHV591
PHV596
PHV592
PHV586
PHV587
PHV588
PHV590
PHV595
PHV589
(c)
(d)
Boiling temperature
for 10 MPa water
Maximum temperature
Modeled temperature
at thermocouple position
Measured temperature
Temperature [°C]
Shear displacement [m]
(d)
100
150
200
250
300
50
50
Thermocouple position
Gouge

Figure 8.

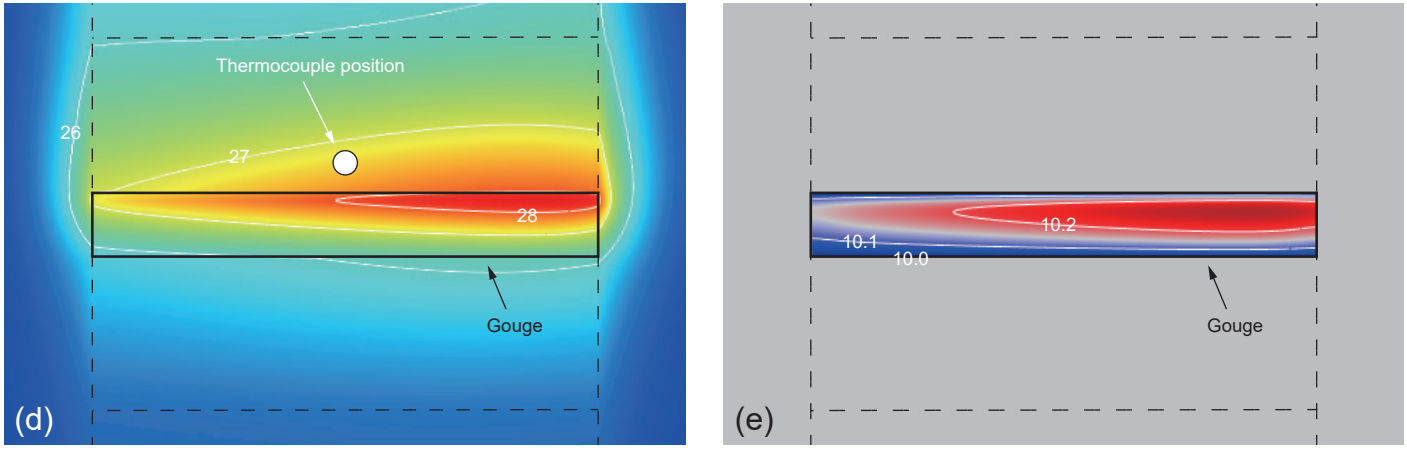
(a)
(d,e)
Equivalent pore pressure
Imposed pore pressure
Imposed effective normal stress
Corrected effective normal stress
Pore pressure [MPa]
Effective normal stress [MPa]
(b)
Corrected friction coefficient
Apparent friction coefficient
Friction coefficient
(c)
Expelled water amount
Axial shortening
Expelled water volume [cc]
Axial shortening [mm]
Shear displacement [m]
Thermocouple position
Gouge
(d)
Gouge
(e)

Figure 9.

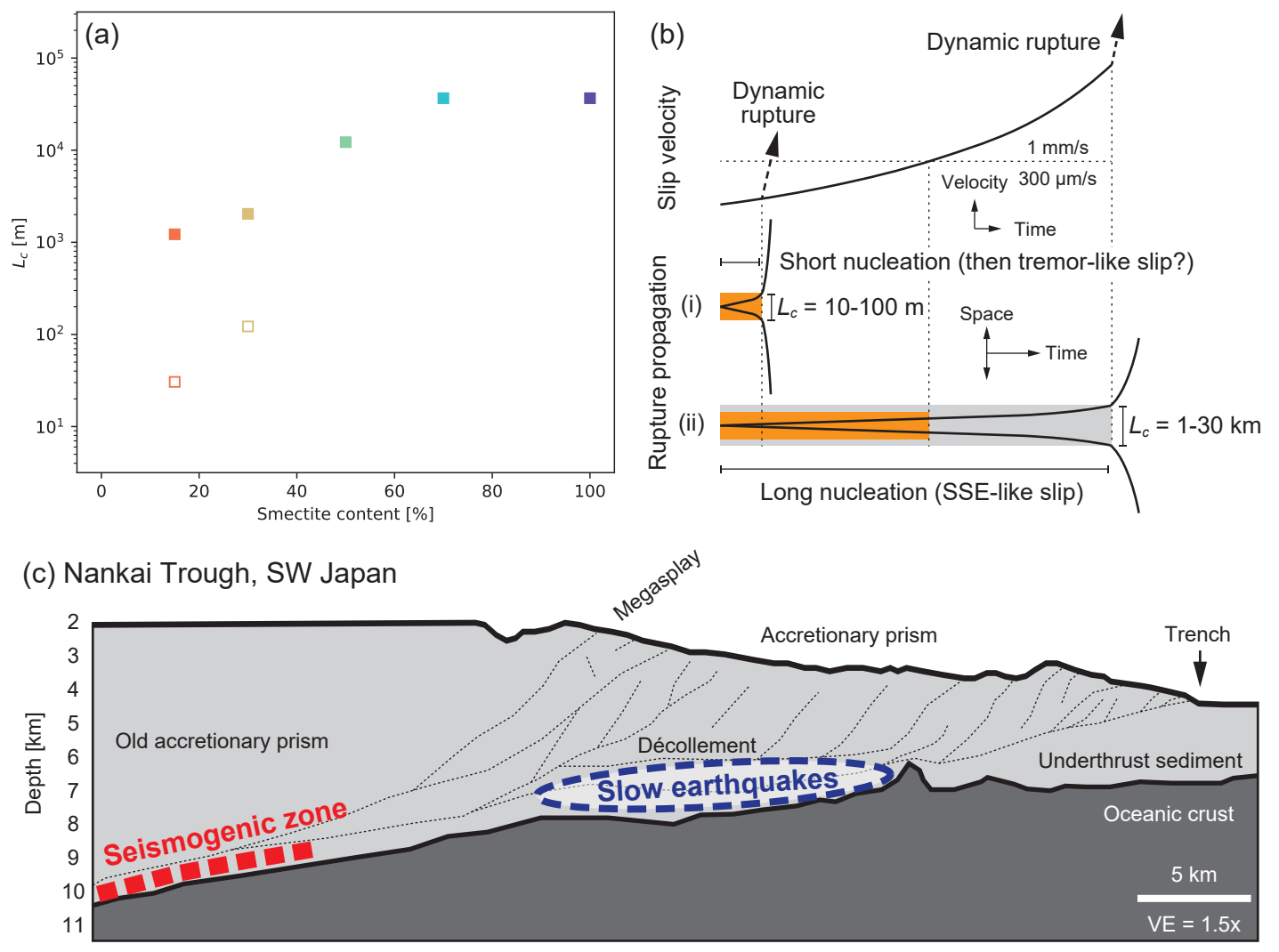
(a)
L_c [m]
10^5
10^4
10^3
10^2
10^1
0
20
40
60
80
100
Smectite content [%]
(b)
Dynamic rupture
Dynamic rupture
Slip velocity
1 mm/s
Velocity
300 μm/s
Time
Short nucleation (then tremor-like slip?)
Rupture propagation
(i)
L_c = 10-100 m
Space
Time
(ii)
L_c = 1-30 km
Long nucleation (SSE-like slip)
(c) Nankai Trough, SW Japan
Megasplay
Accretionary prism
Trench
Depth [km]
2
3
4
5
6
7
8
9
10
11
Old accretionary prism
Décollement
Underthrust sediment
Slow earthquakes
Seismogenic zone
Oceanic crust
5 km
VE = 1.5x